M.F. Lumentut · M.I. Friswell

A smart pipe energy harvester excited by fluid flow and base excitation

Abstract This paper presents electromechanical dynamic modelling of the partially smart pipe structure subject to the vibration responses from fluid flow and input base excitation for generating the electrical energy. We believe that this work shows the first attempt to formulate the unified analytical approach of flow-induced vibrational smart pipe energy harvester in application to the smart sensor-based structural health monitoring systems including those to detect flutter instability. The arbitrary topology of the thin electrode segments located at the surface of the circumference region of the smart pipe has been used so that the electric charge cancellation can be avoided. The analytical techniques of the smart pipe conveying fluid with discontinuous piezoelectric segments and proof mass offset, connected with the standard AC-DC circuit interface, have been developed using the extended charge-type-Hamiltonian mechanics. The coupled field equations reduced from the Ritz method-based weak form analytical approach have been further developed to formulate the orthonormalised dynamic equations. The reduced equations show combinations of the mechanical system of the elastic pipe and fluid flow, electromechanical system of the piezoelectric component, and electrical system of the circuit interface. The electromechanical multi-mode frequency and time signal waveform response equations have also been formulated to demonstrate the power harvesting behaviours. Initially, the optimal power output due to optimal load resistance without the fluid effect is discussed to compare with previous studies. For potential application, further parametric analytical studies of varying partially piezoelectric pipe segments have been explored to analyse the dynamic stability/instability of the smart pipe energy harvester due to the effect of fluid and input base excitation. Further proof between case studies also include the effect of variable flow velocity for optimal power output, 3-D frequency response, the dynamic evolution of the smart pipe system based on the absolute velocity-time waveform signals, and DC power output-time waveform signals.

Keywords: analytical weak form · electromechanical dynamic instability · energy harvesting · fluid-smart structure interactions · piezoelectric · signal analysis · vibration.

1 Introduction

This paper is concerned with the flow-induced vibration of a smart pipe structural system, and considers the physical interactions between the fluid, solid, circuit, and electromechanical systems. The coupled field effect of the fluid flowing through the elastic pipe has shown an interesting phenomenon and has raised some paradoxes until the late 2000s. Since then, the study has been further developed and the issues with possible paradoxes may still unfold in the future. The reason is that the dynamic stability or instability of the pipe conveying fluid depends upon the contributions of boundary conditions, flow velocity, Coriolis and centrifugal effects, fluid gravitation, tensioning, pressurisation, aspirating pipe, etc. Some equations may require to be extended and/or ignored depending upon the applications and experiments. For example, when the

Mikail F Lumentut
School of Civil and Mechanical Engineering, Curtin University, Australia
E-mail: m.lumentut@curtin.edu.au

Michael I Friswell
College of Engineering, Swansea University, United Kingdom
E-mail: m.i.friswell@swansea.ac.uk

dynamic equations of a pipe with certain base supports (constraints) meet their boundary conditions, it does not mean the whole system with flow can be solved correctly because the discharging flow from the pipe due to the work done by fluid can be either considered or ignored. Feodos'ev [1], Housner [2] and Niordson [3] presented the first preliminary mathematical studies for the flow-induced vibration of pipe systems with both end supported. The correct linear equations of motion have been reduced using several different methods to determine buckling instability or divergence. Later, Holmes [4] proved that the flutter instability never occurs when both ends of the pipe conveying the fluid are supported. Indeed, the system with this support condition is conservative. Long before his work was published, Heinrich [5] had developed the mathematical modelling of pipe vibration with flow under the effects of wave propagation and pressurisation. Moreover, Benjamin [6]-[7] presented groundbreaking research work investigating cantilevered pipe dynamics with flow, requiring a non-conservative equations using Hamiltonian mechanics. He showed the occurrence of stability and flutter instability depending upon the increase of the flow velocity. Examples of simplified mathematical studies of the non-conservative effect to analyse the dynamic stability and instability can be seen in Bottema [8] and Smith and Herrmann [9]. Further works have been extensively developed by Gregory and Païdoussis [10]-[11] whose solution techniques showed three methods consisting of quasi-analytical and numerical solutions and partial differential equations with the Galerkin method [12]. They gave a criteria for the dynamic behaviour indicating the system is stable and damped due to small flow velocity but is unstable due to flutter for high flow velocity. Païdoussis and Issid [13] further developed the Newtonian mechanics of the pipes conveying fluid with different boundary conditions under the effects of tension and fluid pressurisation and gravitation. Païdoussis and Li [14] provided comprehensive technical reviews of the systems with flow with many different case studies and solutions. Ruta and Elishakoff [15] examined the shear-deformable pipe conveying fluid with a partial elastic foundation where the critical velocity increased with increasing foundation span over the pipe using higher values of the fluid-to-pipe mass per unit length ratio. Further analytical works for the fluid-pipe structure interaction using the two different conditions of supports with overhang have been developed in [16] where the divergent and flutter instability using Galerkin's method with Duncan's polynomials have been explored to show the optimal critical velocities through various case studies. Moreover, the pipes conveying fluid using various flow effects and solution techniques have been developed using the finite difference method [17], the fast Fourier transform-based spectral element method [18], and the finite element method [19]-[20]. The effect of flow in the three-dimensional pipes conveying fluid with an attached spring and tip mass have been comprehensively investigated using nonlinear dynamic equations [21]-[23]. For almost four decades, Païdoussis with his group [24] has been authoritative in the development of this area. Recent investigation for flow-induced vibration using the aspirating pipe has been developed mathematically in [25] and [24]. Although system modelling has been key for the theoretical studies, major experimental studies have been developed. Kuiper & Metrikine [26] corrected the theoretical works of Païdoussis [25] where the effect of flutter due to the aspirating pipe can occur due to the Coriolis force even without the centrifugal force and the depressurization depends on the inlet flow resulting in the negative pressure range values at the free end of the pipe. As a result, Païdoussis, et al. [27] revisited the issues raised. However, even after this series of published experimental and numerical studies, [28]-[29], specific conclusions about the aspirating pipe have not been finalised.

For the smart structure system, the coupled field effect of the piezoelectric material has shown viable interactions between the electrical, thermal, and mechanical behaviours. In the earlier studies, there have been growing mathematical interests in the applications for piezoelectric structures in structural control-based sensing and actuation systems [30]-[34], shape control-based sensing and actuation under static and dynamic responses [35]-[37], strain-type sensor networks [38]-[39], feedback gain control-based sensor and actuator systems [40–41], thermal effects [37], [42]-[43], and shunt control-based circuit systems [44]-[47]. Over the past decade, smart structures for converting the mechanical energy into electrical energy have shown application in micro-power extraction for the use of extending the battery life and enabling wireless sensor devices. This technique has spurred the development of theoretical solutions of the continuous system modelling such as Rayleigh-Ritz methods [48]-[50], modal analysis method [51], weak-form techniques [52], fully closed-form boundary value methods [53], random analysis [54]-[55], analytical voltage- and charge-type Hamiltonian formulations [56], and electromechanical finite element analysis [57]-[58]. In recent developments to widen the power output frequency bandwidth and to increase power amplitude, complex smart structure power harvesters studied

with various analytical methods have been investigated using the piezoelectric dynamic magnifier with proof mass offset effect [59], the piezoelectric segment system [60]-[61], the multiple piezoelectric bimorph beams connected with different circuit interfaces [62]-[66]. Moreover, the wideband piezoelectric power harvesting system using the charge-type Hamiltonian-based analytical method was developed using shunt control system-based adaptive single piezoelectric bimorph beams with distributed and segmented electrodes [67]-[68]. An aerodynamic system to capture electrical energy has been investigated using the vortex-induced vibration of a tree-inspired system [69], transverse galloping analytical studies [70] and experimental works [71], and flapping flags with two-dimensional inviscid flow [72].

In this paper, the equations of a partially smart pipe conveying fluid with a tip mass offset and base excitation, and connected to the standard AC-DC circuit interface, have been simultaneously formulated using the Ritz method-based weak form analytical approach reduced from the charge-type-Hamiltonian mechanics. Since the smart pipe covered with a thin electrode layer has a uniform cylindrical form, the arbitrary topology of electrode segments was taken into account to avoid electric charge cancellation. For various flow velocities, the effect of dynamic stability/instability of the smart pipe system was analysed using varying discontinuous piezoelectric segments. The orthonormalised dynamic equations were reduced to formulate the power output multi-mode frequency and time signal waveform responses. Currently, there are no previous works developing the proposed theoretical models. Detailed discussions of the parametric analytical studies have been provided to analyse the system response without and with fluid effects and these case studies are discussed extensively. For structural safety, the high pipe displacements at resonance or with the flutter instability can cause fatigue of the pipe and the structural safety should be carefully checked during the detailed design of a particular system. However, flexible piezoelectric elements such as MFCs and EAPap film provide potential solutions for a flexible pipe. Potential application of this concept can be found in the particular design of micro- or meso-scale flexible pipe structure power harvesters under fluid flow for detecting the flutter instability. The smart pipe conveying a fluid may also be applied in a miniature jet flow power harvesting device for smart sensor-based structural health monitoring to detect water levels, flood levels, or the pH level of water including toxicity. Another application is a windsock power harvester device for a smart sensor to monitor wind speed, weather (humidity, temperature, etc), flood/water level, and to charge a battery.

2 Constitutive coupled equations

In Fig. 1a, the smart pipe system with proof mass offset is shown, connected with the harvesting circuit system, and consisting of substructure and piezoelectric layers. Here, the linear piezoelectric beam constitutive equation-based Helmholtz free energy in terms of the 3-1 mode of piezoelectric constant operation and the 3-3 effect of piezoelectric permittivity can be formulated using the stress-electric field relation [56], [73]-[75] as,

$$T_1^{(2)} = \bar{c}_D^{(2)} S_1^{(2)} - g_{31}^{(2)} D_3^{(2)}, \tag{1.1}$$

$$E_3^{(2)} = -g_{31}^{(2)} S_1^{(2)} + \varepsilon_{33}^{S\,-1} D_3^{(2)}. \tag{1.2}$$

where the parameters T, S, E and D represent stress, strain, electric field, and electric displacement, respectively. Moreover, the coefficients c_D, g, and ε indicate modified elastic constant, modified piezoelectric constant and permittivity at constant strain, respectively (Appendix A). Note that each layer of the smart pipe structure is denoted by superscripts, where 1 and 2 represent the substructure and piezoelectric layers respectively. They can be used for stress T, strain S, elastic stiffness c, density ρ, and cross-sectional area A. The linear-elastic constitutive relation for the substructure can be formulated as,

$$T_1^{(1)} = \bar{c}_{11}^{(1)} S_1^{(1)}. \tag{2}$$

In figure 2, the fluid entering the undeformed pipe at point o via a rigid base support is under a steady flow velocity U relative to the pipe. At the same time, the undeformed pipe, located at the fixed reference frame of oXZ, moves in the initial reference frame of $o'XZ$ due to the base vector $\boldsymbol{w}_{base}(t)$ moving from the point o to o'. The position of point p also moves to point p' indicating the same magnitude as the base vector.

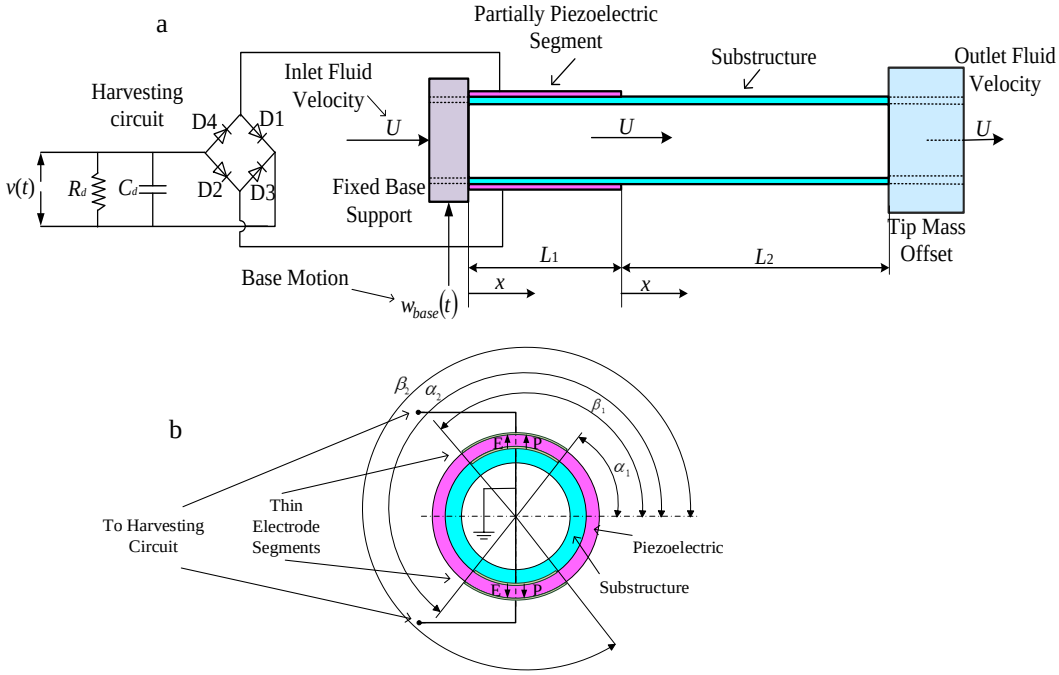

Fig.1 Physical systems: (a) flow-induced vibrational smart pipe structure with tip mass offset and input base excitation connected with circuit interface and (b) cross-sectional smart pipe with arbitrary electrode segments arranged in series connection (example).

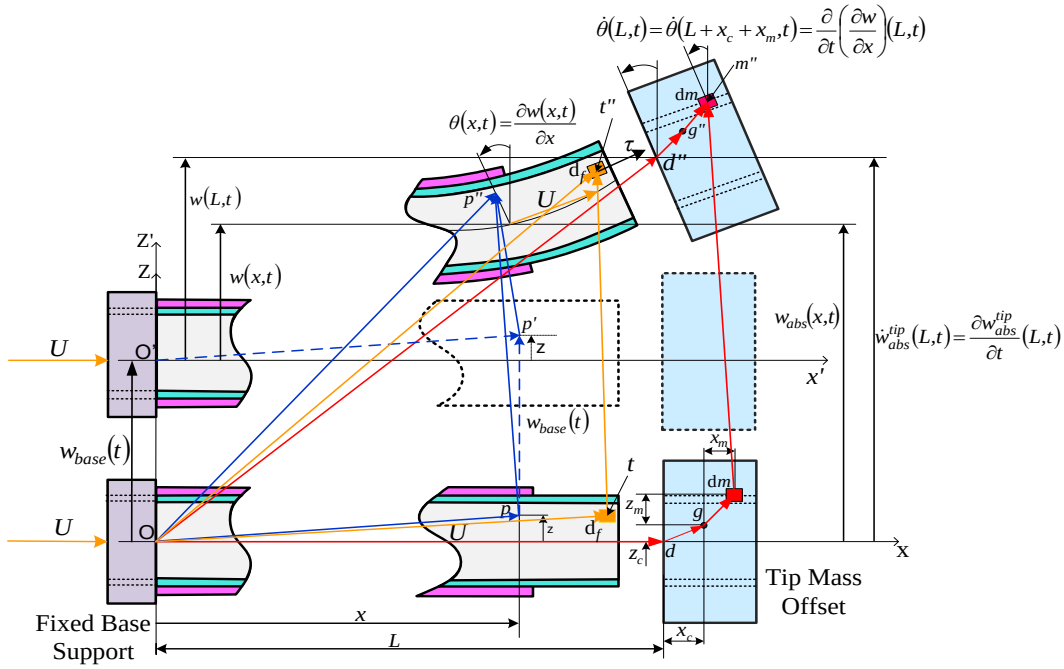

Fig.2 Kinematic motions of the smart pipe structure with tip mass offset under fluid flow and input base excitation.

As the base vector represents the input excitation, the pipe undergoes relative transverse deformation $w(x,t)$ as indicated by point p' moving to the final point p''. The flow velocity U relative to the pipe, which depends on the unit vector tangent $\boldsymbol{\tau}$, is related to the material derivative from the continuum body. It is defined as a time rate of change of physical property for the fluid element flowing through the pipe, while its element also moves from points p to p''. The absolute displacement $w_{abs}(x,t)$ with respect to the deformed pipe is measured from the reference frame of oXZ to the final position. Note that the difference between the absolute

displacement and base vector defines the relative deformation. Since the pipe carries a tip mass with the centroid located at a distance offset from the end of the pipe, the position vectors of the tip mass start from the fixed reference frame *oXZ* to the final differential element of the tip mass at point m''. The offset results in the extra position vector from point of attachment d'' (deformation point of the end of the pipe) to the tip mass centroid at point g''. The tip mass centroid, whose origin is determined from the differential element, has the extra position vector from point g'' to m'' relative to the local point d'' of the local parallel coordinate system of the tip mass structure.

The position vectors $\boldsymbol{R}^{pp''}$, $\boldsymbol{R}^{od}$, $\boldsymbol{R}^{ot}$, $\boldsymbol{R}^{od''}$ and $\boldsymbol{R}^{tt''}$ for the pipe can be defined as,

$$\boldsymbol{R}^{pp''}(x,z,t) = -z\sin\theta(x,t)\boldsymbol{e}_1 + \left(w_{base}(t) + w(x,t)\right)\boldsymbol{e}_3 \ , \tag{3.1}$$

$$\boldsymbol{R}^{od} = L\boldsymbol{e}_1 \ , \ \boldsymbol{R}^{ot} = L\boldsymbol{e}_1 + z\boldsymbol{e}_3 \ , \tag{3.2}$$

$$\boldsymbol{R}^{od''} = \left(L - z\sin\theta(L,t)\right)\boldsymbol{e}_1 + \left(w(L,t) + w_{base}(t) + z\cos\theta(L,t)\right)\boldsymbol{e}_3 \ , \tag{3.3}$$

$$\boldsymbol{R}^{tt''}(L,z,t) = \boldsymbol{R}^{od''} - \boldsymbol{R}^{ot} = -z\theta(L,t)\boldsymbol{e}_1 + \left(w_{base}(t) + w(L,t)\right)\boldsymbol{e}_3 \ . \tag{3.4}$$

Note that small angle $\theta(\cdot,t) = \partial w(\cdot,t)/\partial x$ approximation has be used based on the Taylor's series to give $\sin\theta(\cdot,t) \approx \theta(\cdot,t)$ and $\cos\theta(\cdot,t) \approx 1$.

The unit vector tangential of the fluid element in the pipe can be formulated as,

$$\boldsymbol{\tau} = \frac{\partial\left(z\theta(L,t)\right)}{\partial x}\boldsymbol{e}_1 + \theta(L,t)\boldsymbol{e}_3 \ . \tag{4}$$

Using the Reynolds transport theorem and the material derivative, the fluid element flowing through the pipe can be formulated as,

$$\boldsymbol{v}^f(t) = \left(\frac{\partial \boldsymbol{R}^{pp''}}{\partial t} + U\frac{\partial \boldsymbol{R}^{pp''}}{\partial x}\right) . \tag{5}$$

The absolute velocity vectors for the pipe and tip mass components can be formulated as,

$$\dot{\boldsymbol{w}}_{abs}(x,t) = \left(\dot{w}_{base}(t) + \dot{w}(x,t)\right)\boldsymbol{e_3} \ \text{ and } \ \dot{\boldsymbol{w}}_{abs}^{tip}(L,t) = \left(\dot{w}_{base}(t) + \dot{w}(L,t)\right)\boldsymbol{e_3} \ . \tag{6}$$

The velocity of the elemental tip mass offset can also be formulated as,

$$\begin{aligned}\dot{\boldsymbol{R}}^{mm''}(L,z,t) &= \dot{\boldsymbol{R}}^{od''} + \dot{\boldsymbol{R}}^{d''g''} + \dot{\boldsymbol{R}}^{g''m''} - \dot{\boldsymbol{R}}^{od} - \dot{\boldsymbol{R}}^{dg} - \dot{\boldsymbol{R}}^{gm} \\ &= \left(\dot{w}_{base}(t) + \dot{w}(L,t)\right)\boldsymbol{e}_3 - \dot{\theta}(L,t)\boldsymbol{e}_2 \times \left(z_c\,\boldsymbol{e}_3 + x_c\,\boldsymbol{e}_1\right) - \dot{\theta}(L,t)\boldsymbol{e}_2 \times \left(z_m\,\boldsymbol{e}_3 + x_m\,\boldsymbol{e}_1\right).\end{aligned} \tag{7}$$

The position vector $\boldsymbol{R}^{p'p''}$ can be specified as the relative displacement with respect to the moving base support from reference frame oXZ to $o'X'Z'$ as,

$$\boldsymbol{R}^{p'p''}(x,z,t) = \boldsymbol{R}^{pp''} - \boldsymbol{R}^{pp'} = -z\theta(x,t)\boldsymbol{e_1} + w(x,t)\boldsymbol{e_3} \ . \tag{8}$$

The strain field for all layers can be obtained by differentiating $\boldsymbol{R}^{p'p''}$ with respect to *x* giving the typical Euler-Bernoulli theory as,

$$S_1(x,t) = \frac{\partial\left(\boldsymbol{R}^{p'p''}\cdot\boldsymbol{e}_1\right)}{\partial x} = -z\frac{\partial^2 w(x,t)}{\partial x^2} \ . \tag{9}$$

Note that since all vectors depend on the variables *x* and *t*, they can be utilised at different locations or segments of the smart pipe structure. Further formulations related to the segmented structures are derived in the next section.

3 Fluid-solid-circuit-electromechanical weak form analytical approach

This section formulates the weak form Ritz method using the charge-type Hamilton's principle. The fully coupled field equations consisting of the mechanical system (fluid and solid), electromechanical system (piezoelectricity), and electrical system (circuit interface) are introduced to formulate the orthonormalised dynamic equations. Further solutions of the key equations will be explored in this paper.

3.1. Coupled system of fluid-solid-electromechanical dynamic with harvesting circuit.

The coupled system of the smart pipe conveying fluid for vibration energy harvester can be formulated using the extended charge-type Hamilton's principle to give,

$$\int_{t_1}^{t_2} \delta\left(L_a + W_f\right)\mathrm{d}t = 0 \quad \left.\begin{array}{l} L_a \in \{KE, PE, WE, WC\} \\ W_f \in \{WF_D, WF, WR\} \end{array}\right\} , \tag{10}$$

or

$$\int_{t_1}^{t_2} \left(\delta KE - \delta PE - \delta WE + \delta WF + \delta WF_D - \delta WC + \delta WR\right)\mathrm{d}t = 0 . \tag{11}$$

Each functional energy term in Eq. (11) is expanded in Eqs. (12)-(22). Note that a detailed discussion of the charge-type-based Hamiltonian mechanics was given in [56]. The kinetic energy of the smart pipe conveying fluid and the proof mass offset can be formulated as,

$$\begin{aligned} KE = {} & \frac{1}{2}\int_0^{L_1}\int_{A^{(1)}} \rho^{(1)} \dot{\boldsymbol{R}}^{pp''} \cdot \dot{\boldsymbol{R}}^{pp''}\,\mathrm{d}A^{(1)}\,\mathrm{d}x + \frac{1}{2}\int_0^{L_1}\int_{A^{(2)}} \rho^{(2)} \dot{\boldsymbol{R}}^{pp''} \cdot \dot{\boldsymbol{R}}^{pp''}\,\mathrm{d}A^{(2)}\,\mathrm{d}x \\ & + \frac{1}{2}\int_0^{L_2}\int_{A^{(1)}} \rho^{(1)} \dot{\boldsymbol{R}}^{pp''} \cdot \dot{\boldsymbol{R}}^{pp''}\,\mathrm{d}A^{(1)}\,\mathrm{d}x + \frac{1}{2}\int_0^{L^{tip}}\int_{A^{tip}} \rho^{tip} \dot{\boldsymbol{R}}^{mm''} \cdot \dot{\boldsymbol{R}}^{mm''}\,\mathrm{d}A^{tip}\,\mathrm{d}x_{tip} \\ & + \frac{1}{2}\int_0^{L_1}\int_{A^f} \rho^f \boldsymbol{v}^f(t)\cdot \boldsymbol{v}^f(t)\,\mathrm{d}A^f\,\mathrm{d}x + \frac{1}{2}\int_0^{L_2}\int_{A^f} \rho^f \boldsymbol{v}^f(t)\cdot \boldsymbol{v}^f(t)\,\mathrm{d}A^f\,\mathrm{d}x . \end{aligned} \tag{12}$$

Parameters $\rho^{(1)}, \rho^{(2)}, \rho^{tip}$ and ρ^f represent the mass densities of the substructure, the piezoelectric, the proof mass offset, and the fluid components, respectively. Eq. (12) can be extended by substituting Eqs. (3.1), (5) and (7). After manipulation and simplification, Eq. (12) can be reformulated in terms of the variational form to give,

$$\begin{aligned} \int_{t_1}^{t_2} \delta KE = {} & \int_{t_1}^{t_2}\Bigg\{\int_0^L \Bigg(\sum_{n=1}^{2} H_n(x) I_{2n}\dot{\theta}(x,t)\delta\dot{\theta}(x,t) + \sum_{n=1}^{2} H_n(x) I_{0n}\dot{w}(x,t)\delta\dot{w}(x,t)\Bigg)\mathrm{d}x \\ & + H_2(x)\Big(I_0^{tip}\dot{w}(L_2,t)\delta\dot{w}(L_2,t) + I_2^{tip}\dot{\theta}(L_2,t)\delta\dot{\theta}(L_2,t) + I_0^{tip}x_c\left(\dot{w}(L_2,t)\delta\dot{\theta}(L_2,t) + \delta\dot{w}(L_2,t)\dot{\theta}(L_2,t)\right)\Big) \\ & + \int_0^L\int_{A^f}\sum_{n=1}^{2} H_n(x)\Big(\rho^f\left(\dot{w}(x,t)\delta\dot{w}(x,t) + z^2\dot{\theta}(x,t)\delta\dot{\theta}(x,t) + \dot{w}_{base}(t)\delta\dot{w}(x,t)\right) \\ & - \rho^f U\left(2z^2\frac{\partial\dot{\theta}(x,t)}{\partial x}\delta\theta(x,t) + 2\frac{\partial\dot{w}(x,t)}{\partial x}\delta w(x,t)\right) \\ & + \rho^f U^2\left(\theta(x,t)\delta\theta(x,t) + \frac{\partial(z\theta(x,t))}{\partial x}\delta\frac{\partial(z\theta(x,t))}{\partial x}\right)\Big)\mathrm{d}A^f\,\mathrm{d}x \\ & + \int_{A^f}\rho^f U H_2(x)\left(z^2\dot{\theta}(L_2,t)\delta\theta(L_2,t) + \dot{w}(L,t)\delta w(L_2,t) + \dot{w}_{base}(t)\delta w(L_2,t)\right)\mathrm{d}A^f\Bigg\}\mathrm{d}t \quad . \end{aligned} \tag{13}$$

Note that based on the consistency of the physical geometry in Fig. 1, Heaviside functions for $H_1(x)=H(x)-H(x-L_1)$ and $H_2(x)=H(x)-H(x-L_2)$ are introduced to model the two segmented structures with different mode shapes along the x-axis. It is also important to note here that although the fluid flows within the uniform internal pipe section, the Heaviside functions on the fluid part are also utilised due to different modes at each segment. Parameters I_{0n} and I_{2n} represent the zeroth and second mass moments of inertia of the segmented structures whereas parameters I_0^{tip} and I_2^{tip} represent the zeroth and second mass moments of the tip mass. Also note that details of the mathematical expressions for the dynamical structure and proof mass offset as shown in the first six terms of Eq. (13) can be found in [58]. They were reduced since the relative displacement $w(x,t)$ is defined as the difference between the absolute displacement $w_{abs}(x,t)$ and the base excitation $w_{base}(t)$. The potential energy or strain energy of the structure can be formulated as,

$$PE = \frac{1}{2}\int_0^{L_1}\int_{A^{(1)}} S_1^{(1)}T_1^{(1)}\mathrm{d}A^{(1)}\mathrm{d}x + \frac{1}{2}\int_0^{L_1}\int_{A^{(2)}} S_1^{(2)}T_1^{(2)}\mathrm{d}A^{(2)}\mathrm{d}x + \frac{1}{2}\int_0^{L_2}\int_{A^{(1)}} S_1^{(1)}T_1^{(1)}\mathrm{d}A^{(1)}\mathrm{d}x \quad . \tag{14}$$

The variation of strain energy can be further formulated by substituting Eqs. (1.1)-(2) and (9) into Eq. (14) and taking into account the segmented structures and electrodes, as

$$\int_{t_1}^{t_2}\delta PE\,\mathrm{d}t = \int_{t_1}^{t_2}\left\{\int_0^{L}\sum_{n=1}^{2} H_n(x)C_{tn}\frac{\partial^2 w(x,t)}{\partial x^2}\delta\frac{\partial^2 w(x,t)}{\partial x^2}\mathrm{d}x - \int_0^{L}\int_{A^{(2)}}\sum_{h=1}^{2} zg_{31}^{(2)}D_3^{(2)}G_h(\gamma)H_1(x)\delta\frac{\partial^2 w(x,t)}{\partial x^2}\mathrm{d}A^{(2)}\mathrm{d}x\right\}\mathrm{d}t\,. \tag{15}$$

Parameter C_{tn} represents the arbitrary stiffness coefficient of the segmented structures. Note that the Heaviside functions $G_1(\gamma)=H(\gamma-\alpha_1)-H(\gamma-\beta_1)$ and $G_2(\gamma)=H(\gamma-\alpha_2)-H(\gamma-\beta_2)$ are introduced since the two segmented electrodes are located on the circumference region of the piezoelectric layer in the polar coordinate system. Parameter D_3 depends on the segmented system, and is $D_3^{(2)} = q_{11}\Big/\int_{\alpha_1}^{\beta_1}\int_0^{L_1} r_3\mathrm{d}x\mathrm{d}\gamma\ \forall G_1(\gamma)$ and $D_3^{(2)} = q_{12}\Big/\int_{\alpha_2}^{\beta_2}\int_0^{L_1} r_3\mathrm{d}x\mathrm{d}\gamma\ \forall G_2(\gamma)$. These are used in the forthcoming reduced equations. Note that q_{11} and q_{12} represent internal charge parameters in the electrode layers of the piezoelectric circuit (for example, series connection).

The electrical energy term for the piezoelectric elements can be formulated to give,

$$WE = \frac{1}{2}\int_0^{L_1}\int_{A^{(2)}} E_3^{(2)}D_3^{(2)}\mathrm{d}A^{(2)}\mathrm{d}x \quad . \tag{16}$$

Eq. (16) can be extended using Eq. (1.2) as,

$$\int_{t_1}^{t_2}\delta WE\,\mathrm{d}t = \int_{t_1}^{t_2}\left\{\int_0^{L}\int_{A^{(2)}}\sum_{h=1}^{2}\left(-zg_{31}^{(2)}\frac{\partial^2 w(x,t)}{\partial x^2} + \varepsilon_{33}^{S^{-1}}D_3^{(2)}\right)G_h(\gamma)H_1(x)\delta D_3^{(2)}\mathrm{d}A^{(2)}\mathrm{d}x\right\}\mathrm{d}t\,. \tag{17}$$

The non-conservative work on the system due to the input base excitation can be stated as,

$$\int_{t_1}^{t_2}\delta WF\mathrm{d}t = \int_{t_1}^{t_2}\left\{-\int_0^{L}\sum_{n=1}^{2} H_n(x)I_{0n}\delta w(x,t)\mathrm{d}x - I_0^{tip}x_c H_2(x)\delta\theta(L_2,t) - I_0^{tip}H_2(x)\delta w(L_2,t)\right\}\ddot{w}_{base}(t)\mathrm{d}t\,. \tag{18}$$

Note that detail of the mathematical expressions of Eq. (18) can be found in [58].

The variational form of energy gained due to fluid flow at the free end of the pipe can be formulated as,

$$\int_{t_1}^{t_2}\delta WF_D\,\mathrm{d}t = \int_{t_1}^{t_2}\left\{-M^f U\left(\frac{\partial \boldsymbol{R}^{tt''}}{\partial t} + U\boldsymbol{\tau}\right)\cdot\delta\boldsymbol{R}^{tt''}\right\}\mathrm{d}t \quad . \tag{19}$$

Since the end of the smart pipe structure with the offset proof mass is free to move, Eq. (19) must be taken into account ($WF_D \neq 0$) leading to a non-conservative system due to the discharged fluid. M^f is the mass of fluid per unit length. However, if both ends are fixed, Eq. (19) is ignored ($WF_D = 0$), and this assumption has been used in many previous papers related to a pipe conveying a fluid [6],[10], [24]. Also note that Eq. (19) implies two physical behaviours of the smart pipe conveying fluid. If U is positive and sufficiently small, the free motion of the pipe will be damped. This occurs when the first part of the multiplication inside the curly brackets is much larger than the second part resulting in $WF_D < 0$ due to the Coriolis force. However, if U is positive and large, the free motion of the pipe will be amplified because the pipe will gain energy from the flow. This occurs when the second part has the opposite signs during a cycle of oscillation resulting in $WF_D > 0$. In such situations, the system will have a dynamic instability and the pipe shows a dragging, lagging motion that has been demonstrated in experimental and theoretical studies [6]-[7], [10]-[11], [24]. After manipulation and simplification, Eq. (19) can be reformulated using Eqs. (3.4) and (4) to give,

$$\int_{t_1}^{t_2} \delta WF_D \,\mathrm{d}t = -\int_{t_1}^{t_2} \Bigg\{ \int_{A^f} \rho^f U H_2(x)\Big(z^2 \dot{\theta}(L_2,t)\delta\theta(L_2,t) + \dot{w}_{base}(t)\delta w(L_2,t) + \dot{w}(L_2,t)\delta w(L_2,t)\Big)\mathrm{d}A^f$$

$$- \rho^f U^2 \int_0^L \int_{A^f} \sum_{n=1}^{2} H_n(x)\left(\frac{\partial(z\theta(x,t))}{\partial x}\delta\frac{\partial(z\theta(x,t))}{\partial x} + \theta(x,t)\delta\theta(x,t)\right)\mathrm{d}A^f \,\mathrm{d}x$$

$$- \int_0^L \sum_{n=1}^{2} H_2(x)\left(I_2^f U^2 \frac{\partial^2\theta(x,t)}{\partial x^2}\delta\theta(x,t) + M^f U^2 \frac{\partial\theta(x,t)}{\partial x}\delta w(x,t)\right)\mathrm{d}x \Bigg\}\mathrm{d}t\,. \tag{20}$$

The electrical energy of the capacitor in terms of the tuning circuit can be formulated as,

$$\delta WC = \frac{1}{C_d} q_2(t)\delta q_2(t)\,. \tag{21}$$

The electrical work dissipated by the resistor can be stated as,

$$\delta WR = -R_d \dot{q}_3(t)\delta q_3(t)\,. \tag{22}$$

In terms of the variational operations, the functional energy forms in Eq. (7) can be prescribed as the continuous differentiable functions of virtual displacements, electric displacement and charge for the whole system that can be stated as,

$$L_a = L_a\begin{pmatrix} \dot{w}(x,t), \dot{w}(L,t), \dfrac{\partial\dot{w}(x,t)}{\partial x}, \dfrac{\partial\dot{w}(L,t)}{\partial x}, w(x,t), w(L,t), \\ \dfrac{\partial w(x,t)}{\partial x}, \dfrac{\partial w(L,t)}{\partial x}, \dfrac{\partial^2 w(x,t)}{\partial x^2}, D_3^{(2)}(z,t), q_2(t) \end{pmatrix}, \tag{23.1}$$

$$W_f = W_f\left(w(x,t), \frac{\partial w(L,t)}{\partial x}, w(L,t), w(x,t), \frac{\partial w(x,t)}{\partial x}, \frac{\partial(z\theta(x,t))}{\partial x}, q_3(t)\right)\,. \tag{23.2}$$

Equations (23.1) and (23.2) can be further formulated using total differential equations as,

$$\delta L_a = \frac{\partial L_a}{\partial\dot{w}(x,t)}\delta\dot{w}(x,t) + \frac{\partial L_a}{\partial\dot{w}(L,t)}\delta\dot{w}(L,t) + \frac{\partial L_a}{\partial\left(\frac{\partial\dot{w}}{\partial x}(x,t)\right)}\delta\left(\frac{\partial\dot{w}}{\partial x}(x,t)\right) + \frac{\partial L_a}{\partial\left(\frac{\partial\dot{w}}{\partial x}(L,t)\right)}\delta\left(\frac{\partial\dot{w}}{\partial x}(L,t)\right)$$

$$+ \frac{\partial L_a}{\partial w(x,t)}\delta w(x,t) + \frac{\partial L_a}{\partial w(L,t)}\delta w(L,t) + \frac{\partial L_a}{\partial\left(\frac{\partial w(x,t)}{\partial x}\right)}\delta\left(\frac{\partial w(x,t)}{\partial x}\right) + \frac{\partial L_a}{\partial\left(\frac{\partial w(L,t)}{\partial x}\right)}\delta\left(\frac{\partial w(L,t)}{\partial x}\right)$$

$$+ \frac{\partial L_a}{\partial\left(\frac{\partial^2 w(x,t)}{\partial x^2}\right)}\delta\left(\frac{\partial^2 w(x,t)}{\partial x^2}\right) + \frac{\partial L_a}{\partial D_3^{(2)}(z,t)}\delta D_3^{(2)}(z,t) + \frac{\partial L_a}{\partial q_2(t)}\delta q_2(t), \tag{24.1}$$

$$\delta W_f = \frac{\partial W_f}{\partial w(x,t)}\delta w(x,t) + \frac{\partial W_f}{\partial\left(\frac{\partial w}{\partial x}(L,t)\right)}\delta\left(\frac{\partial w}{\partial x}(L,t)\right) + \frac{\partial W_f}{\partial w(L,t)}\delta w(L,t) + \frac{\partial W_f}{\partial w(x,t)}\delta w(x,t)$$

$$+ \frac{\partial W_f}{\partial\left(\frac{\partial w}{\partial x}(x,t)\right)}\delta\left(\frac{\partial w(x,t)}{\partial x}\right) + \frac{\partial W_f}{\partial\left(\frac{\partial(z\theta(x,t))}{\partial x}\right)}\delta\left(\frac{\partial(z\theta(x,t))}{\partial x}\right) + \frac{\partial W_f}{\partial q_3(t)}\delta q_3(t)\,. \tag{24.2}$$

To formulate dynamical weak form equation, the extended variational principle can be developed corresponding to the virtual relative transverse displacement field due to the fluid, the solid and the virtual electrical charge due to piezoelectricity and the harvesting circuit. The weak form-based Ritz method [76]-[77] can be further formulated for the solution, and requires a test function that is a piecewise continuous function over the entire domain of the coupled system. The function must meet continuity requirements and boundary conditions. After manipulation and simplification, the electromechanical weak form of Eq. (11) can be formulated using Eqs. (13), (15), (17), (18), (20)-(22) in terms of Eqs. (24.1)-(24.2) to give,

$$
\begin{aligned}
&\int_{t_1}^{t_2}\Bigg[\int_0^L\sum_{n=1}^{2}H_n(x)\Bigg\{\left(I_{2n}+I_2^f\right)\frac{\partial\ddot{w}(x,t)}{\partial x}\frac{\partial\delta w(x,t)}{\partial x}+\left(\left(I_{0n}+M^f\right)\ddot{w}(x,t)+\left(I_{0n}+M^f\right)\ddot{w}_{base}(t)\right)\delta w(x,t)\\
&+2I_2^fU\frac{\partial^2\dot{w}(x,t)}{\partial x^2}\frac{\partial\delta w(x,t)}{\partial x}+2M^fU\frac{\partial\dot{w}(x,t)}{\partial x}\delta w(x,t)+I_2^fU^2\frac{\partial^3 w(x,t)}{\partial x^3}\frac{\partial\delta w(x,t)}{\partial x}\\
&+M^fU^2\frac{\partial^2 w(x,t)}{\partial x^2}\delta w(x,t)+C_{tn}\frac{\partial^2 w(x,t)}{\partial x^2}\frac{\partial^2\delta w(x,t)}{\partial x^2}\Bigg\}\mathrm{d}x+\int_0^L\left(\eta_1 q_{11}+\eta_2 q_{12}\right)H_1(x)\frac{\partial^2\delta w(x,t)}{\partial x^2}\mathrm{d}x\\
&+H_2(x)\left\{x_cI_0^{tip}\frac{\partial\ddot{w}(L_2,t)}{\partial x}+I_0^{tip}\ddot{w}(L_2,t)+I_0^{tip}\ddot{w}_{base}(t)\right\}\delta w(L_2,t)\\
&+H_2(x)\left\{I_2^{tip}\frac{\partial\ddot{w}(L_2,t)}{\partial x}+x_cI_0^{tip}\ddot{w}(L_2,t)+x_cI_0^{(tip)}\ddot{w}_{base}(t)\right\}\delta\frac{\partial w(L_2,t)}{\partial x}\\
&+\left\{\int_0^L\eta_1H_1(x)\frac{\partial^2 w(x,t)}{\partial x^2}\mathrm{d}x+\frac{q_{11}(t)}{C_{v1}}\right\}\delta q_{11}(t)+\left\{\int_0^L\eta_2H_1(x)\frac{\partial^2 w(x,t)}{\partial x^2}\mathrm{d}x+\frac{q_{12}(t)}{C_{v2}}\right\}\delta q_{12}(t)\\
&+\frac{q_2(t)\delta q_2(t)}{C_d}+R_d\dot{q}_3(t)\delta q_3(t)\Bigg]\,\mathrm{d}t=0\,.
\end{aligned}
\tag{25}
$$

Each coefficient in Eq. (25) is given in Appendices B, C, and D. Applying KCL for the internal piezoelectric connection and harvesting circuit in Fig. 1 gives the electric charge equations as,

$$
q_1=q_{11}=q_{12}\ ,\quad q_1=q_2+q_3\,. \tag{26}
$$

Note that the series connection was used as an example for the internal piezoelectric connection. The variable q_2 in Eq. (25) can be eliminated for simplicity using,

$$
\frac{q_2(t)}{C_d}\delta q_2(t)=\frac{q_1(t)}{C_d}\delta q_1(t)-\frac{q_3(t)}{C_d}\delta q_1(t)-\frac{q_1(t)}{C_d}\delta q_3(t)+\frac{q_3(t)}{C_d}\delta q_3(t)\ . \tag{27}
$$

The normalised eigenfunction series form can be formulated as,

$$
w(x,t)=\sum_{r=1}^{m}\hat{W}_r(x)w_r(t)\quad . \tag{28}
$$

Substituting Eq. (28) into Eq. (25) gives the first dynamic equation representing the smart pipe conveying fluid under transverse bending as

$$
\begin{aligned}
&\sum_{q=1}^{m}\Bigg\{\sum_{r=1}^{m}\Bigg[\Bigg(\int_0^L\sum_{n=1}^{2}H_n(x)\left(\left(I_2+I_2^f\right)\frac{\mathrm{d}\hat{W}_q(x)}{\mathrm{d}x}\frac{\mathrm{d}\hat{W}_r(x)}{\mathrm{d}x}+\left(I_0+M^f\right)\hat{W}_q(x)\hat{W}_r(x)\right)\mathrm{d}x+H_2(x)\Bigg(I_0^{tip}\hat{W}_q(L_2)\hat{W}_r(L_2)+x_cI_0^{tip}\hat{W}_q(L_2)\frac{\mathrm{d}\hat{W}_r(L_2)}{\mathrm{d}x}\\
&+x_cI_0^{tip}\frac{\mathrm{d}\hat{W}_q(L_2)}{dx}\hat{W}_r(L_2)+I_2^{tip}\frac{\mathrm{d}\hat{W}_q(L_2)}{\mathrm{d}x}\frac{\mathrm{d}\hat{W}_r(L_2)}{\mathrm{d}x}\Bigg)\ddot{w}_r(t)+\int_0^L\sum_{n=1}^{2}H_n(x)\left(2I_2^fU\frac{\mathrm{d}\hat{W}_q(x)}{\mathrm{d}x}\frac{\mathrm{d}^2\hat{W}_r(x)}{\mathrm{d}x^2}+2M^fU\hat{W}_q(x)\frac{\mathrm{d}\hat{W}_r(x)}{\mathrm{d}x}\right)\mathrm{d}x\dot{w}_r(t)\\
&+\int_0^L\sum_{n=1}^{2}H_n(x)\left(C_{tn}\frac{\mathrm{d}^2\hat{W}_q(x)}{\mathrm{d}x^2}\frac{\mathrm{d}^2\hat{W}_r(x)}{\mathrm{d}x^2}+M^fU^2\hat{W}_q(x)\frac{\mathrm{d}^2\hat{W}_r(x)}{\mathrm{d}x^2}+I_2^fU^2\frac{\mathrm{d}\hat{W}_q(x)}{\mathrm{d}x}\frac{\mathrm{d}^3\hat{W}_r(x)}{\mathrm{d}x^3}\right)\mathrm{d}xw_r(t)\\
&+\int_0^L(\eta_1+\eta_2)H_1(x)\frac{\mathrm{d}^2\hat{W}_q}{\mathrm{d}x^2}q_1(t)\mathrm{d}x+\Bigg(\int_0^L\sum_{n=1}^{2}H_n(x)\left(I_{0n}+M^f\right)\hat{W}_q(x)\mathrm{d}x\\
&+H_2(x)\left(x_cI_0^{tip}\frac{\mathrm{d}\hat{W}_q(L_2)}{\mathrm{d}x}+I_0^{tip}\hat{W}_q(L)\right)\Bigg)\ddot{w}_{base}(t)\Bigg\}\delta w_q(t)=0\ \cdot
\end{aligned}
\tag{29}
$$

The second and third equations represent the piezoelectric and harvesting circuit forms, respectively that can be formulated as,

$$
\left\{\sum_{r=1}^{m}\int_0^L(\eta_1+\eta_2)H_1(x)\frac{\mathrm{d}^2\hat{W}_r(x,t)}{\mathrm{d}x^2}\mathrm{d}xw_r(t)+\left(\frac{C_{v1}+C_{v2}}{C_{v1}C_{v2}}+\frac{1}{C_d}\right)q_1(t)-\frac{q_3(t)}{C_d}\right\}\delta q_1(t)=0\,, \tag{30.1}
$$

$$\left\{R_d\dot{q}_3(t)+\frac{q_3(t)}{C_d}-\frac{q_1(t)}{C_d}\right\}\delta q_3(t)=0\,. \tag{30.2}$$

For more compact system equations, the constitutive equations from Eqs. (29), (30.1)-(30.2) can also be simplified into matrix form by including the mechanical damping coefficients to give,

$$\overbrace{M_{qr}^m\ddot{w}_r+C_{qr}^m\dot{w}_r+K_{qr}^m w_r}^{\text{Mechanical System}}-\overbrace{P_qP_r\gamma C_d w_r+P_q\gamma q_3}^{\text{Electromechanical and Circuit System}}=-\overbrace{\left(M_{qr}^f\ddot{w}_r+C_{qr}^f\dot{w}_r+K_{qr}^f w_r\right)}^{\text{Hydro-Elastodynamic System}}-\overbrace{\left(Q_q^f+Q_q^m\right)\ddot{w}_{base}(t)}^{\text{Base Excitation due to Fluid and Structure}}\,, \tag{31.1}$$

$$\overbrace{R_d\dot{q}_3+P_{Cd}q_3+P_r\gamma w_r}^{\text{Electromechanical and Circuit System}}=0\,. \tag{31.2}$$

Alternatively, Eqs. (31.1)-(31.2) can be reformulated into matrix form as,

$$\begin{bmatrix}M_{qr}^m+M_{qr}^f & 0\\ 0 & 0\end{bmatrix}\begin{Bmatrix}\ddot{w}_r\\ \ddot{q}_3\end{Bmatrix}+\begin{bmatrix}C_{qr}^m+C_{qr}^f & 0\\ 0 & R_d\end{bmatrix}\begin{Bmatrix}\dot{w}_r\\ \dot{q}_3\end{Bmatrix}+\begin{bmatrix}K_{qr}^m+K_{qr}^f-P_qP_r\gamma C_d & P_q\gamma\\ P_r\gamma & P_{Cd}\end{bmatrix}\begin{Bmatrix}w_r\\ q_3\end{Bmatrix}=\begin{Bmatrix}-\left(Q_q^f+Q_q^m\right)\ddot{w}_{base}(t)\\ 0\end{Bmatrix}, \tag{32}$$

where,

$$M_{qr}^m=\int_0^L\sum_{n=1}^2 H_n(x)\left(I_{2n}\frac{\mathrm{d}\hat{W}_q(x)}{\mathrm{d}x}\frac{\mathrm{d}\hat{W}_r(x)}{\mathrm{d}x}+I_{0n}\hat{W}_q(x)\hat{W}_r(x)\right)\mathrm{d}x+I_0^{tip}H_2(x)\hat{W}_q(L_2)\hat{W}_r(L_2)$$
$$+H_2(x)\left(x_cI_0^{tip}\hat{W}_q(L_2)\frac{d\hat{W}_r(L_2)}{dx}+x_cI_0^{tip}\frac{\mathrm{d}\hat{W}_q(L_2)}{\mathrm{d}x}\hat{W}_r(L_2)+I_2^{tip}\frac{\mathrm{d}\hat{W}_q(L_2)}{\mathrm{d}x}\frac{\mathrm{d}\hat{W}_r(L_2)}{\mathrm{d}x}\right), \tag{33.1}$$

$$M_{qr}^f=\int_0^L\sum_{n=1}^2 H_n(x)\left(M^f\hat{W}_q(x)\hat{W}_r(x)+I_2^f\frac{\mathrm{d}\hat{W}_q(x)}{\mathrm{d}x}\frac{\mathrm{d}\hat{W}_r(x)}{\mathrm{d}x}\right)\mathrm{d}x\,, \tag{33.2}$$

$$C_{qr}^m=c_vM_{qr}^m+c_dK_{qr}^m\,, \tag{33.3}$$

$$C_{qr}^f=\int_0^L\sum_{n=1}^2 H_n(x)\left(2M^fU\hat{W}_q(x)\frac{\mathrm{d}\hat{W}_r(x)}{\mathrm{d}x}+2I_2^fU\frac{\mathrm{d}\hat{W}_q(x)}{\mathrm{d}x}\frac{\mathrm{d}^2\hat{W}_r(x)}{\mathrm{d}x^2}\right)\mathrm{d}x\,, \tag{33.4}$$

$$K_{qr}^m=\int_0^L\sum_{n=1}^2 C_{tn}H_n(x)\frac{\mathrm{d}^2\hat{W}_q(x)}{\mathrm{d}x^2}\frac{\mathrm{d}^2\hat{W}_r(x)}{\mathrm{d}x^2}\mathrm{d}x\,, \tag{33.5}$$

$$K_{qr}^f=\int_0^L\sum_{n=1}^2 H_n(x)\left(M^fU^2\hat{W}_q(x)\frac{\mathrm{d}^2\hat{W}_r(x)}{\mathrm{d}x^2}+I_2^fU^2\frac{\mathrm{d}\hat{W}_q(x)}{\mathrm{d}x}\frac{\mathrm{d}^3\hat{W}_r(x)}{\mathrm{d}x^3}\right)\mathrm{d}x\,, \tag{33.6}$$

$$P_r=\int_0^L(\eta_1+\eta_2)H_1(x)\frac{\mathrm{d}^2\hat{W}_r(x)}{\mathrm{d}x^2}\mathrm{d}x\,,\quad P_q=\int_0^L(\eta_1+\eta_2)H_1(x)\frac{\mathrm{d}^2\hat{W}_q(x)}{\mathrm{d}x^2}\mathrm{d}x\,, \tag{33.7}$$

$$P_{Cd}=\frac{1}{C_d}(1-\gamma)\,,\quad \gamma=\frac{C_{v1}C_{v2}}{\left(C_{v1}C_d+C_{v2}C_d+C_{v1}C_{v2}\right)}, \tag{33.8}$$

$$Q_q^f=\int_0^L\sum_{n=1}^2 M^fH_n(x)\hat{W}_q(x)\mathrm{d}x\,,\quad Q_q^m=\int_0^L\sum_{n=1}^2 I_0H_n(x)\hat{W}_q(x)\mathrm{d}x+H_2(x)\left(I_0^{tip}\hat{W}_q(L_2)+x_cI_0^{tip}\frac{\mathrm{d}\hat{W}_q(L_2)}{\mathrm{d}x}\right). \tag{33.9}$$

Note that there are four major technical aspects that can be outlined as followed,

1. Eq. (32) represents the coupled field equations of fluid-solid-circuit-electromechanical system.
2. If some parameters of the piezoelectric system such as P_r, P_q and P_{Cd} and the proof mass offset terms M_{qr}^m ($x_cI_0^{tip}$) and Q_q^m ($I_2^{tip}, x_cI_0^{tip}$), are ignored, then Eq. (32) can be reduced to similar form to that of previous works of a fluid flow-induced pipe vibration system as shown by the examples in [6], [10], [13], [24].

3. The Coriolis effect due to fluid flow through the pipe can be seen in the first term of the C_{qr}^{f} matrix.
4. The centrifugal effect due to the fluid flow through the pipe can also be seen in the first term of the K_{qr}^{f} matrix.

Note that with the Euler-Bernoulli assumptions, the second mass moment of inertias of the pipe structure and the fluid (I_2 and I_2^f) are ignored. Also, the fluid gravitation and pressurization at the beginning of derivations were excluded for simplicity due to the relative meso-scale pipe system. The parameter $\hat{W}_r(.)$ representing the normalised eigenfunction for the Euler-Bernoulli pipe structure is assumed to be

$$\hat{W}_r(x)=\frac{W_r(x)}{\left(\int_0^L\sum_{n=1}^{2}I_{0n}H_n(x)W_r(x)^2\mathrm{d}x+H_2(x)\left(I_0^{tip}W_r(L_2)^2+2x_cI_0^{tip}W_r(L_2)\frac{\mathrm{d}W_r}{\mathrm{d}x}(L_2)+I_2^{tip}\left(\frac{\mathrm{d}W_r}{\mathrm{d}x}(L_2)\right)^2\right)\right)^{1/2}}\quad ,r=1,2,..,\ m\quad . \tag{34}$$

The function $W_r(.)$ can be obtained from the generalized space-dependent Ritz eigenfunctions as,

$$W_r(x)=\sum_{k=1}^{m}c_{kr}W_k(x)\quad ,\quad r=1,2,...,m\quad . \tag{35}$$

Note that the accurate mode shape $W_k(x)$ reduced from the closed-form boundary value technique can be found in Appendix E and the generalized Ritz coefficient c_{kr} is the eigenvector matrix. To obtain the coefficients, Eq. (28) was initially formulated as $w(x,t)=\sum_{r=1}^{m}c_rW_r(x)e^{i\omega t}$ so that Eq. (32) can be rearranged by only considering the characteristic mechanical equation $\sum_{r=1}^{m}\left[K_{qr}-\omega^2M_{qr}\right]c_r=0$, $q=1,2,....,m$. The Ritz coefficients c_r for the mechanical transverse bending form can be manipulated into matrix form corresponding with the eigenvalues for each column of the matrix. Corresponding to Eqs. (32), the orthonormalisations can now be further proven by using Eq. (34) in terms of the orthogonality property of the mechanical dynamic equations as,

$$\begin{aligned}&\int_0^L\sum_{n=1}^{2}I_{0n}H_n(x)\hat{W}_q(x)\hat{W}_r(x)\mathrm{d}x+H_2(x)\Bigg(I_0^{tip}\hat{W}_q(L_2)\hat{W}_r(L_2)+x_cI_0^{tip}\hat{W}_q(L_2)\frac{\mathrm{d}\hat{W}_r(L_2)}{\mathrm{d}x}\\&+x_cI_0^{tip}\frac{\mathrm{d}\hat{W}_q(L_2)}{\mathrm{d}x}\hat{W}_r(L_2)+I_2^{tip}\frac{\mathrm{d}\hat{W}_q(L_2)}{\mathrm{d}x}\frac{\mathrm{d}\hat{W}_r(L_2)}{\mathrm{d}x}\Bigg)=\delta_{qr}=\begin{cases}0 & if\ \ r\neq q\\1 & if\ \ r=q\end{cases}\ ,\end{aligned} \tag{36.1}$$

$$\int_0^L\sum_{n=1}^{2}C_{tn}H_n(x)\frac{\mathrm{d}^2\hat{W}_q(x)}{\mathrm{d}x^2}\frac{\mathrm{d}^2\hat{W}_r(x)}{\mathrm{d}x^2}\mathrm{d}x=\delta_{qr}\omega_r{}^2=\begin{cases}0 & if\ \ r\neq q\\\omega_r{}^2 & if\ \ r=q\end{cases}. \tag{36.2}$$

Two Rayleigh mechanical damping coefficients in Eq. (33.3) can determined by applying orthonormality. Detailed derivations are given in [53]. The mass proportional damping term due to air friction can be estimated as,

$$\begin{aligned}&\int_0^L c_vI_0\hat{W}_q(x)\hat{W}_r(x)\mathrm{d}x+c_vI_0^{tip}\hat{W}_q(L)\hat{W}_r(L)+x_cc_vI_0^{tip}\hat{W}_q(L)\frac{\mathrm{d}\hat{W}_r(L)}{\mathrm{d}x}\\&+x_cc_vI_0^{tip}\frac{\mathrm{d}\hat{W}_q(L)}{\mathrm{d}x}\hat{W}_r(L)+c_vI_2^{tip}\frac{\mathrm{d}\hat{W}_q(L)}{\mathrm{d}x}\frac{\mathrm{d}\hat{W}_r(L)}{\mathrm{d}x}=c_v\delta_{qr}=\begin{cases}0 & if\ \ r\neq q\\c_v & if\ \ r=q\end{cases}\end{aligned}\quad . \tag{37}$$

The stiffness proportional damping term due to internal friction of damping stress of the smart pipe structure can be estimated as,

$$\int_0^L c_d C_s \frac{\mathrm{d}^2 \hat{W}_q(x)}{\mathrm{d}x^2}\frac{\mathrm{d}^2 \hat{W}_r(x)}{\mathrm{d}x^2}\mathrm{d}x = c_d \delta_{qr}\omega_r{}^2 = \begin{cases} 0 & if\ \ r \neq q \\ c_d \omega_r{}^2 & if\ \ r = q \end{cases} \quad . \tag{38}$$

Therefore, Rayleigh mechanical damping coefficients can simply be reduced to give,

$$C_{qr} = c_v \delta_{qr} + c_d\ \delta_{qr}\ \omega_r{}^2 = 2\delta_{qr}\zeta_r\,\omega_r \quad . \tag{39}$$

where δ_{rq} is the Kronecker delta. Note that the functions $\hat{W}_\mathrm{r}(x)$ and $\hat{W}_\mathrm{q}(x)$ are the normalised mode shapes. Applying the orthonormalisation from Eqs. (36.1)-(36.2) and (37)-(38) into Eq. (32) gives the fluid-smart pipe system equations in terms of the index notation as,

$$\begin{aligned}&\left(\delta_{qr} + \hat{M}_{qr}^f\right)\ddot{w}_r(t) + \left(2\delta_{qr}\zeta_r\omega_r + \hat{C}_{qr}^f\right)\dot{w}_r(t) + \left(\delta_{qr}\omega_r{}^2 + \hat{K}_{qr}^f\right)w_r(t) \\ &\quad - \gamma C_d P_q\, P_r\, w_r(t) + P_q \gamma q_3(t) = -\left(Q_q^f + Q_q^m\right)\ddot{w}_{base}(t)\ ,\end{aligned} \tag{40.1}$$

$$R_d \dot{q}_3(t) + P_{Cd}\, q_3(t) + \gamma P_r\, w_r(t) = 0 \quad . \tag{40.2}$$

The two dependent electromechanical equations, Eqs. (40.1)-(40.2), show the coupled field system of fluid-smart structure interaction with a standard harvesting circuit. At this case, since those equations have been normalised, the fluid parameters can be reduced to give,

$$\hat{M}_{qr}^f = \int_0^L \sum_{n=1}^{2} M^f H_n(x)\hat{W}_q(x)\hat{W}_r(x)\mathrm{d}x\ , \quad \hat{K}_{qr}^f = \int_0^L \sum_{n=1}^{2} M^f U^2 H_n(x)\hat{W}_q(x)\frac{\mathrm{d}^2 \hat{W}_r(x)}{\mathrm{d}x^2}\mathrm{d}x\ , \tag{41.1}$$

$$\hat{C}_{qr}^f = \int_0^L \sum_{n=1}^{2} 2M^f U H_n(x)\hat{W}_q(x)\frac{\mathrm{d}\hat{W}_r(x)}{\mathrm{d}x}\mathrm{d}x\ . \tag{41.2}$$

Note that the other parameters can be seen in Eq. (33). The characteristic electromechanical dynamic equation with the *n*-th degree-of-freedom can be formulated using the index notation as,

$$\det\begin{bmatrix} \left(\underset{(n\times n)}{2\delta_{qr}\zeta_r\omega_r} + \underset{(n\times n)}{\hat{C}_{qr}^f}\right) j\omega - \left(\underset{(n\times n)}{\delta_{qr}} + \underset{(n\times n)}{\hat{M}_{qr}^f}\right)\omega^2 + \left(\underset{(n\times n)}{\delta_{qr}\omega_r{}^2} + \underset{(n\times n)}{\hat{K}_{qr}^f} - \gamma C_d \underset{(n\times 1)}{P_q}\underset{(1\times n)}{P_r}\right) & \underset{(n\times 1)}{P_q\gamma} \\ \underset{(1\times n)}{\gamma P_r} & \underset{(1\times 1)}{j\omega R_d} + \underset{(1\times 1)}{P_{Cd}} \end{bmatrix} = 0\ . \tag{42}$$

Note that once each parameter was identified using the properties of the eigenfunction, the complex driving frequency ω can be calculated using the incremental values of flow velocity U. The Routh-Hurwitz stability criterion can be used to determine the complex polynomial roots of ω and these can be displayed in the Argand diagram.

Laplace transformations are used to give the transfer functions of the multi-mode electromechanical equations. After simplification, the electric charge FRFs can be formulated in terms of the index notation as,

$$\frac{q_3(j\omega)}{-\omega^2 w_{base} e^{j\omega\, t}} = \frac{\left[\gamma \underset{(1\times n)}{P_r} \underset{(n\times n)}{\Phi}\left(\underset{(n\times 1)}{Q_q^f} + \underset{(n\times 1)}{Q_q^m}\right)\right]}{\left[\underset{(1\times 1)}{P_{Cd}} + j\omega \underset{(1\times 1)}{R_d} - \gamma^2 \underset{(1\times n)}{P_r} \underset{(n\times n)}{\Phi} \underset{(n\times 1)}{P_q}\right]}\ , \tag{43}$$

where:

$$\Phi = \left[\underset{(n\times n)}{\delta_{qr}\,\omega_r{}^2} + \underset{(n\times n)}{\hat{K}_{qr}^f} - \gamma C_d \underset{(n\times 1)}{P_q}\underset{(1\times n)}{P_r} - \omega^2\left(\underset{(n\times n)}{\delta_{qr}} + \underset{(n\times n)}{\hat{M}_{qr}^f}\right) + j\omega\left(\underset{(n\times n)}{2\delta_{qr}\,\zeta_r\,\omega_r} + \underset{(n\times n)}{\hat{C}_{qr}^f}\right)\right]^{-1}\ . \tag{44}$$

n represents the number of degrees of freedom in Eq. (43), related to a number of normalised mode shapes. Other multimode FRFs relations can also be formulated. Here, the multi-mode electric current FRFs can be formulated as,

$$\frac{i_3(j\omega)}{-\omega^2 w_{base} e^{j\omega t}} = j\omega \frac{q_3(j\omega)}{-\omega^2 w_{base} e^{j\omega t}} \quad . \tag{45}$$

The voltage FRFs across the resistor or capacitor of the harvesting circuit can be formulated as,

$$\frac{v(j\omega)}{-\omega^2 w_{base} e^{j\omega t}} = j\omega R_d \frac{q_3(j\omega)}{-\omega^2 w_{base} e^{j\omega t}} \quad . \tag{46}$$

The power FRFs across the resistor and capacitor can also be formulated respectively as,

$$\frac{P_{Res}(j\omega)}{\left(-\omega^2 w_{base} e^{j\omega t}\right)^2} = -\omega^2 R_d \frac{q_3(j\omega)^2}{\left(-\omega^2 w_{base} e^{j\omega t}\right)^2} \quad , \tag{47.1}$$

$$\frac{P_{Cap}(j\omega)}{\left(-\omega^2 w_{base} e^{j\omega t}\right)^2} = -j\omega^3 R_d{}^2 C_d \frac{q_3(j\omega)^2}{\left(-\omega^2 w_{base} e^{j\omega t}\right)^2} \quad . \tag{47.2}$$

As an example, the optimal load resistance is formulated using Eq. (47.1) as,

$$R_d^{opt} = \left| -\frac{j}{\omega}\left(P_{Cd} - \gamma^2 P_r \Phi P_q\right) \right| . \tag{48}$$

Note that the parameter Φ is seen in Eq. (44). The optimal power output can be formulated by substituting back Eq. (48) into Eq. (47.1) in terms of Eq. (43).

3.2. Electrical signal waveform with Standard Harvesting AC-DC Interface Circuit

This section discusses the conversion of AC electrical signal output from the piezoelectric component via the electrode segments into a DC electrical signal output from the full-bridge rectifier. The DC output can be further smoothed using an RC circuit. In Fig. 3, the signal waveforms show different forms from the system parts such as the AC voltage of the piezoelectric, DC signal voltages via rectifier and capacitor, and DC currents via a capacitor and load resistance.

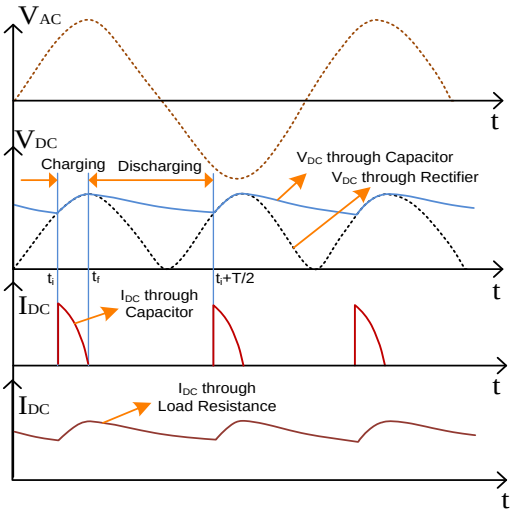

Fig.3 Time waveforms of the standard harvesting circuit

a. Current flowing with interval $t_i < t < t_f$ indicating the charging time over every half-cycle of the frequency.

The system equations with harvesting DC rectifier and smoothing RC circuit can be reformulated with slight modification in Eqs. (40.1)-(40.2). The following equations of the coupled system response during the period of charging can be formulated as,

$$\left(\delta_{qr} + \hat{M}_{qr}^{f}\right)\ddot{w}_r(t) + \left(2\delta_{qr}\zeta_r\omega_r + \hat{C}_{qr}^{f}\right)\dot{w}_r(t) + \left(\delta_{qr}\omega_r{}^2 + \hat{K}_{qr}^{f}\right)w_r(t) + P_q q_1(t) = -\left(Q_q^f + Q_q^m\right)\ddot{w}_{base}(t), \tag{49.1}$$

$$v_d + P_V q_1(t) + P_r\, w_r(t) = 0 \ , \tag{49.2}$$

where $P_V = (C_{v1} + C_{v2})/C_{v1}C_{v2}$. Note that the first and second terms in Eq. (49.2) were introduced by replacing the first and second terms from Eq. (40.2). They can be obtained by removing Eqs. (21)-(22) and introducing the new electrical work done $\delta WFr = v_d(t)\delta q_1(t)$ in the Hamiltonian functional energy. Differentiating Eq. (49.2) with respect to time gives,

$$\dot{v}_d + P_V \dot{q}_1(t) + P_r \dot{w}_r(t) = 0 . \tag{50}$$

The harvesting DC circuit equation can be formulated as,

$$\dot{q}_1(t) - C_d \dot{v}_d - \frac{v_d}{R_d} = 0 . \tag{51}$$

After substituting parameter $q_1(t)$ from Eq. (49.2) into Eq. (49.2) and parameter $\dot{q}_1(t)$ from Eq. (51) into Eq. (50), the state space representation of the multi-mode response system can be formulated to give,

$$\frac{\mathrm{d}}{\mathrm{d}t}\begin{Bmatrix} w_r(t) \\ \dot{w}_r(t) \\ v_d \end{Bmatrix} = \begin{bmatrix} a_{11} & a_{12} & a_{13} \\ a_{21} & a_{22} & a_{23} \\ a_{31} & a_{32} & a_{33} \end{bmatrix} \begin{Bmatrix} w_r(t) \\ \dot{w}_r(t) \\ v_d \end{Bmatrix} + \begin{Bmatrix} b_1 \\ b_2 \\ b_3 \end{Bmatrix}, \tag{52}$$

where: $a_{11} = a_{13} = a_{31} = 0$, $a_{12} = \delta_{qr}$, $b_1 = b_3 = 0$, (53.1)

$$b_2 = -\frac{\left(Q_q^f + Q_q^m\right)\ddot{w}_{base}(t)}{\left(\delta_{qr} + \hat{M}_{qr}^f\right)}, \quad a_{21} = -\frac{\left(\delta_{qr}\omega_r^{\,2} + \hat{K}_{qr}^f\right)}{\left(\delta_{qr} + \hat{M}_{qr}^f\right)} + \frac{P_q P_r}{P_V\left(\delta_{qr} + \hat{M}_{qr}^f\right)}, \; a_{22} = -\frac{\left(2\delta_{qr}\zeta_r\omega_r + \hat{C}_{qr}^f\right)}{\left(\delta_{qr} + \hat{M}_{qr}^f\right)}, \tag{53.2}$$

$$a_{23} = \frac{P_q}{P_V\left(\delta_{qr} + \hat{M}_{qr}^f\right)}, \quad a_{32} = -\frac{P_r}{\left(P_V C_d + 1\right)}, \quad a_{33} = -\frac{1}{\left(R_d C_d + \dfrac{R_d}{P_V}\right)}. \tag{53.3}$$

b. Current flowing with interval $t_f < t < t_i + T/2$ indicating the discharging times every half-cycle of the frequency.

The harvesting circuit during the period of discharging can be formulated as,

$$C_d \dot{v}_d + \frac{v_d}{R_d} = 0 . \tag{54}$$

The solution of Eq. (54) can be formulated as,

$$v_d(t) = v_d(t_f)\exp\left(\frac{-(t - t_f)}{C_d R_d}\right). \tag{55}$$

Thus, the current and voltage waveform signals during the charging and discharging periods can be predicted using Eqs. (52) and (55).

4 Results and discussion

This section discusses the effect of the fluid flow inside the smart pipe with an offset proof mass. The investigation of dynamic stability or instability using the first four coupled modes highlights the physical phenomena of the smart pipe conveying fluid. The dynamic evolution of the smart pipe system over one period for particular frequencies will also be discussed. This section also includes a discussion of the power harvesting frequency and time signal waveform responses. For the material properties, the smart pipe system is composed of the substructure and piezoelectric layers as shown in Table 1. The piezoelectric material used here was PZT PSI-5A4E. The geometry parameters of length (L), inner and outer radii (r_1 and r_2) of the substructure (elastomer) and inner and outer radii (r_2 and r_3) of the piezoelectric were set to 150 mm, 6 mm and 7.6 mm, and 7.6 mm and 7.7 mm, respectively. Note that the outer radius of the substructure layer is the same value as the inner radius of the piezoelectric layer. The dimensions of the tip mass offset such as length l_t, inner and outer radii (r_{t1} and r_{t2}) were set to 8 mm and 10 mm and 7.6 mm, respectively. The mass of fluid per unit length M^f was set to 0.11 kg/m. The angles of circumference electrode segments were variable for the upper and lower regions of the smart pipe. The input base acceleration was chosen to be 3 m/s^2. Also, the discontinuous piezoelectric segments were also variable. The effect of the variable geometry will be shown later. Again, all dimension parameters are shown in Fig. 1.

Table 1. Material properties

Material properties	Piezoelectric	Elastomer	Fluid
Young's modulus, $\bar{c}_{11}$ (GPa)	66	0.025	-
Density, ρ (kg/m^3)	7800	1200	1000
Piezoelectric constant, d_{31} (pm/V)	-190	-	-
Permittivity, ε_{33}^{T} (F/m)	1800 ε_o	-	-
permittivity of free space, ε_o (pF/m)	8.854	-	-

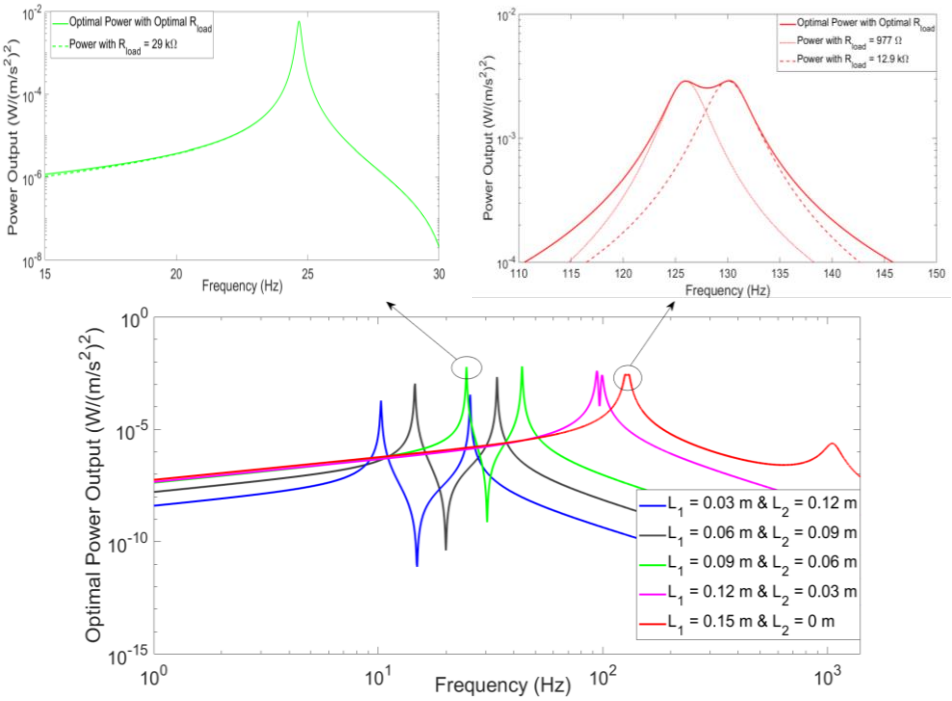

Fig. 4. Optimal power harvesting FRFs under optimal load resistance without fluid effect using electrode segment (β_1-α_1=144° & β_2-α_2=144°) and variable length piezoelectric segment.

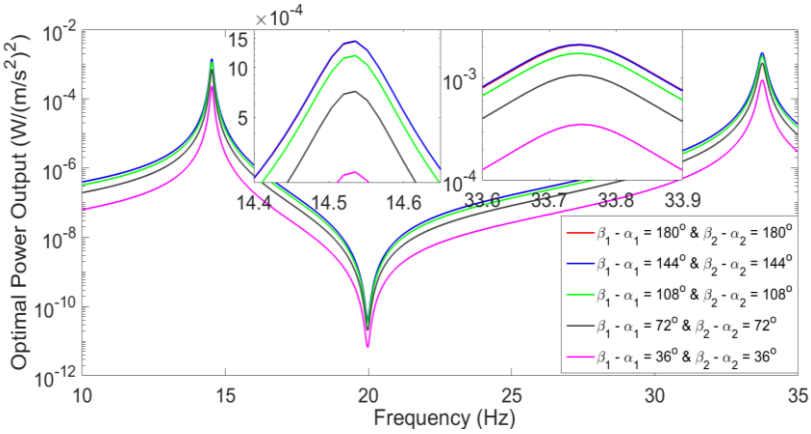

Fig. 5. Optimal power harvesting FRFs under optimal load resistance without fluid effect using a partial piezoelectric segment (L_1=0.06 m & L_2=0.09 m) and variable electrode angle.

In Fig. 4, the trend of the first two modes of the optimal power harvesting frequency responses under optimal load resistance without fluid effect shows the essential aspect for identifying the potential use of different piezoelectric segments. For this case, the optimal load resistance as shown in Eq. (48) was used by removing fluid parts. The two examples of the optimal responses can be seen in the use of the partial piezoelectric segments (L_1=0.09m & L_2=0.06m) and (L_1=0.15m & L_2=0m). Rayleigh damping coefficients of 0.5 rad/s (c_v) and 2e-5 s/rad (c_d) were

chosen for this study. It is found that a significant shift of the resonances from the short to open circuit conditions predominantly occurs for the distributed piezoelectric structure or segment (L_1=0.15m & L_2=0 m). The contribution of the piezoelectric length (L_1=0.15m & L_2=0 m) clearly affects wider optimal responses compared with the other segments. The power responses with two different load resistances overlap with the optimal power response representing strong electromechanical coupling. However, the segment (L_1=0.15m & L_2=0m) for fluid flow does not show an effective option due to very high critical flow velocity as shown next. More detailed discussion of the optimal responses using different geometry and material properties that particularly affect the weak and strong electromechanical coupling can be found in [53].

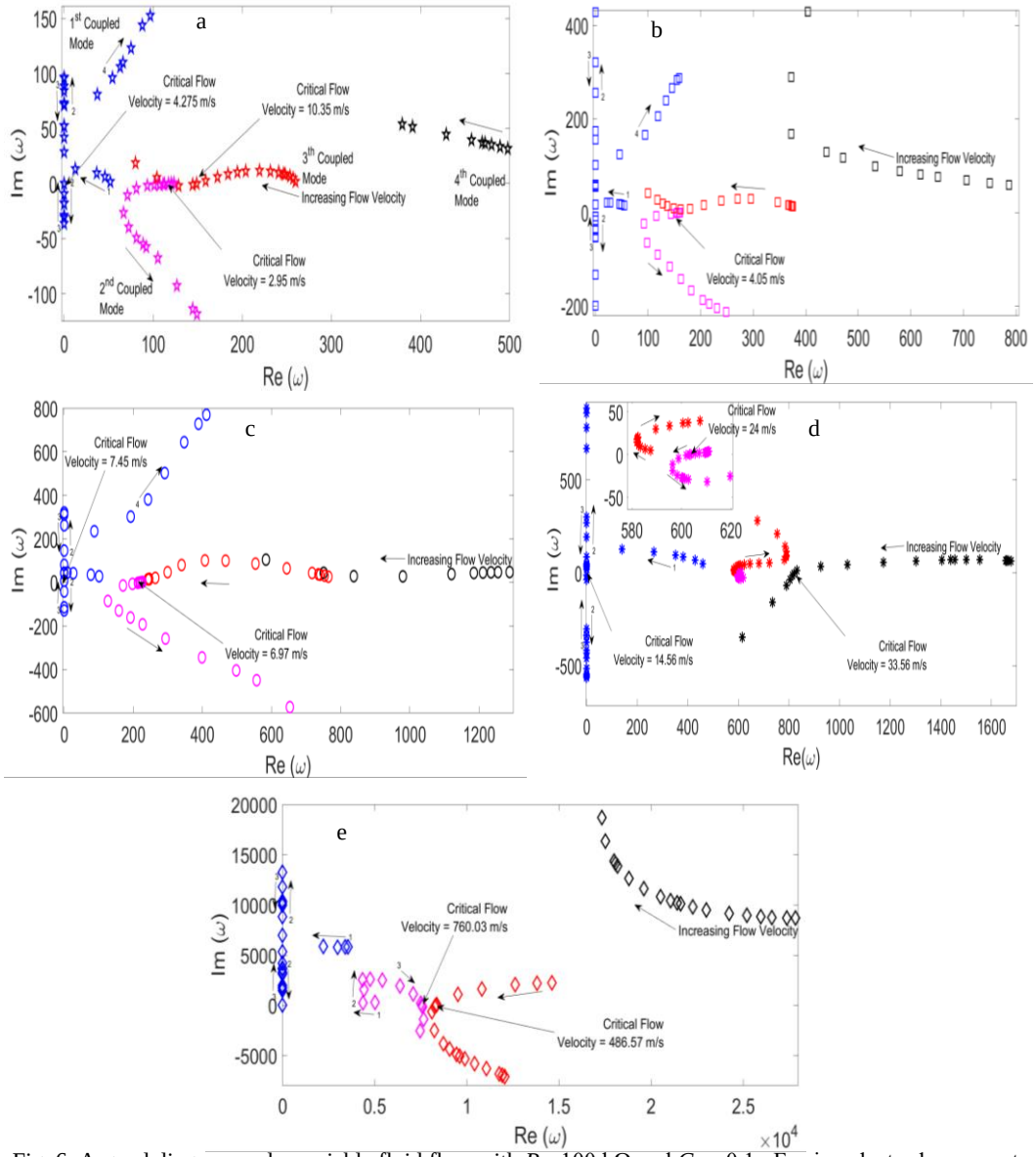

Fig. 6. Argand diagram under variable fluid flow with R_d=100 kΩ and C_d = 0.1 μF using electrode segment (β_1-α_1=144° and β_2-α_2=144°) and partially piezoelectric segment: (a) L_1=0.03m & L_2=0.12 m, (b) L_1=0.06m & L_2=0.09 m, (c) L_1=0.09m & L_2=0.06 m, (d) L_1=0.12m & L_2=0.03 m, (e) L_1=0.15m & L_2=0 m.

For many previous power harvesting research publications, the frequency response system under short and open circuit conditions shows similar behaviour. The difference between the present study and previous works is the different physical geometry of the structure. Most previous works have used a piezoelectric unimorph or bimorph beam. Thus, the aim of presenting Fig. 4 is to ensure the present study has similar trends to the established previous studies. Note that the power responses shown in Fig. 4 used the angle of the electrode circumference segment (β_1-α_1=144° & β_2-α_2=144°) representing the optimal amplitude. This can be proved in Fig. 5 where the particular piezoelectric segment (L_1=0.06m & L_2=0.09m) with variable electrode circumference segment was

chosen as an example. Also note that the electrode segments chosen here have symmetrical geometry between the lower and upper portions of the cross-sectional pipe as shown in Fig. 1b. For example, the electrode segment at upper portion with α_1=18° and β_1=162° gives a difference of 144°. For lower portion, the electrode segments with α_1=198° and β_1=342° also gives a difference of 144°. The complete electrode angles for upper portion are set as α_1=0°, 18°, 36°, 54°, and 72° corresponding to β_1=180°, 162°, 144°, 126°, and 108°. The complete electrode angles for the lower portion are set to α_2=180°, 198°, 216°, 234°, and 252° corresponding to β_2=360°, 342°, 324°, 306°, and 288°. It is noted here that the chosen particular piezoelectric and electrode segments of the smart pipe structure are obviously related to the analysis of the system with the fluid flow effect.

For observing the effect of the smart pipe conveying fluid, the Argand diagram is an essential tool to identify whether the predicted system is unstable. In Fig. 6, the locus points in the Argand diagram for five different piezoelectric segments for the first four coupled modes show different characteristic responses with increasing flow velocities. The electrode segment (β_1-α_1=144° & β_2-α_2=144°) was utilized as it gave the optimal response. Note that the term, "coupled mode" means the system with different frequencies having the combined physical aspects of fluid, solid, and electromechanical systems. For example, it is clearly seen in Fig. 6a that the smart pipe conveying fluid at the first coupled mode observes divergent instability after reaching the critical flow velocity of 4.275 m/s. However, this situation does not occur any longer where the system becomes stable. The instability at the second mode occurs by flutter beyond the critical flow velocity of 2.95 m/s. At the third coupled mode, the system dynamics initially gains stability, but loses it by flutter after reaching the critical flow velocity of 10.35 m/s. On the smart pipe system, it appears that the second mode reached the flutter first where it predominantly affects the whole frequency domain and also depends on the imaginary value that moves faster and higher than other modes. Further proof can be discussed next using the absolute velocity-time waveform signals. Moreover, the fourth coupled modes tend to give stability during operation of the system response to flow velocity. The segments (L_1=0.06m & L_2=0.09m) and (L_1=0.09m & L_2=0.06m) shown in Figs. (6b) and (6c) demonstrate the potential and effective options for the pipe conveying fluid for power harvesting applications. The reason is that the smart pipe requires reasonable lower onset of flutter instability and lower critical velocity value (Hopf bifurcation). The smart pipe having divergent instability may not be a good choice since its natural dynamic behaviour shows static instability that means the pipe velocity grows continuously without oscillation. For power harvesting, oscillation is one of the important aspects to continuously generate electrical energy.

Again further proof of the dynamic instability behaviour of the system can be seen in Fig. 7. Here, the case study of the three different piezoelectric segments is given as example. The absolute velocities at the tip end of elastic pipe using particular fluid flow velocities show the evolution of time waveform responses. Starting with the occurrence of the beating response, Fig. 7a shows the resonance frequency of the smart pipe having similar response to that of the fluid system because the beating phenomenon occurs when the system approaches the critical flow velocity. A slightly higher critical velocity can give an initial flutter response as shown in Fig. 7b. The divergent instability as shown in Fig. 7c occurs. However, the use of the piezoelectric segment (L_1=0.03m & L_2=0.12m) can give the mixed flutter-divergent instability as shown in Fig. 7c. But, the trend shows predominantly divergence over the time domain where the response with a very high amplitude grows without oscillation and bound. This situation can also be proved from Fig. 6a where particular imaginary value of divergent instability response (slightly beyond its critical flow velocity) at the first mode approaches to overlap with the imaginary value of the flutter instability response. Note that the absolute velocity means the total velocity from the relative motion of the elastic pipe and base excitation. With increasing fluid velocities, the absolute velocity of the elastic pipe becomes flutter (response grows continuously with oscillation and without bound) as shown in Fig. 7d.

Fig. 8a shows a stable response below the critical flow velocity. However, it becomes a beating response on reaching the critical flow velocity. However, the system responses appear to change to the flutter instability, as shown in the series of events in Figs. 8c-d. In Fig. 9a with the partially piezoelectric segment (L_1=0.09m & L_2=0.06m), the stable response occurs at below the critical flow velocity. Again the beating response occurs at the critical flow velocity as shown in Fig. 9b. Then, as seen in Fig. 9c, with just a slightly higher flow velocity than its critical value, the dynamic instability occurs by a flutter response (oscillation without bound). There is still the mixed beating response during the formation of the flutter instability. It should be remarked here

that if the flow velocity increases further, as shown in Fig. 9d, the fully flutter response of elastic smart pipe will also continue to increase.

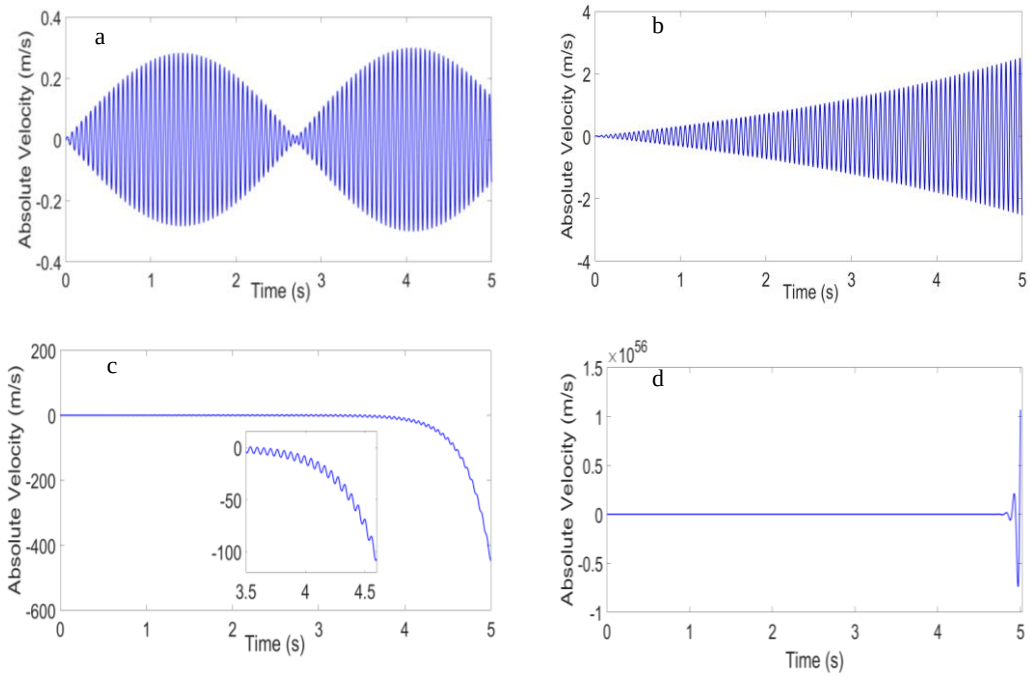

Fig.7. Evolution of the absolute velocity-time waveform signals using piezoelectric segment (L_1=0.03 m & L_2=0.12 m) and electrode segment (β_1-α_1=144° & β_2-α_2=144°) with R_d=100 kΩ and C_d = 0.1 μF under fluid velocity and resonance excitation: (a) U=2.93 m/s with 18.29 Hz, (b) U=3.35 m/s with 18.38 Hz, (c) U=4.37 m/s with 17.69 Hz, (d) U=9 m/s with 11.42 Hz.

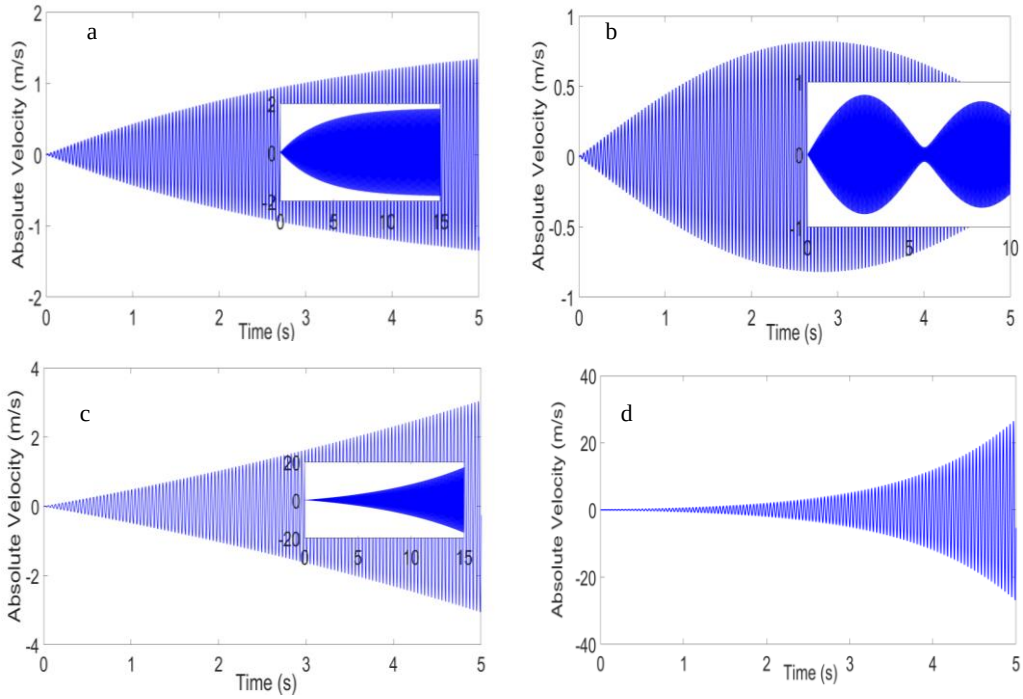

Fig.8. Evolution of the absolute velocity-time waveform signals using piezoelectric segment (L_1=0.06m & L_2=0.09 m) and electrode segment (β_1-α_1=144° & β_2-α_2=144°) with R_d=100 kΩ and C_d = 0.1 μF under fluid velocity and resonance excitation: (a) U=3.75 m/s with 25.60 Hz, (b) U=4.06 m/s with 25.20 Hz, (c) U=4.25 m/s with =25.23 Hz, (d) U=5 m/s with 24.62 Hz.

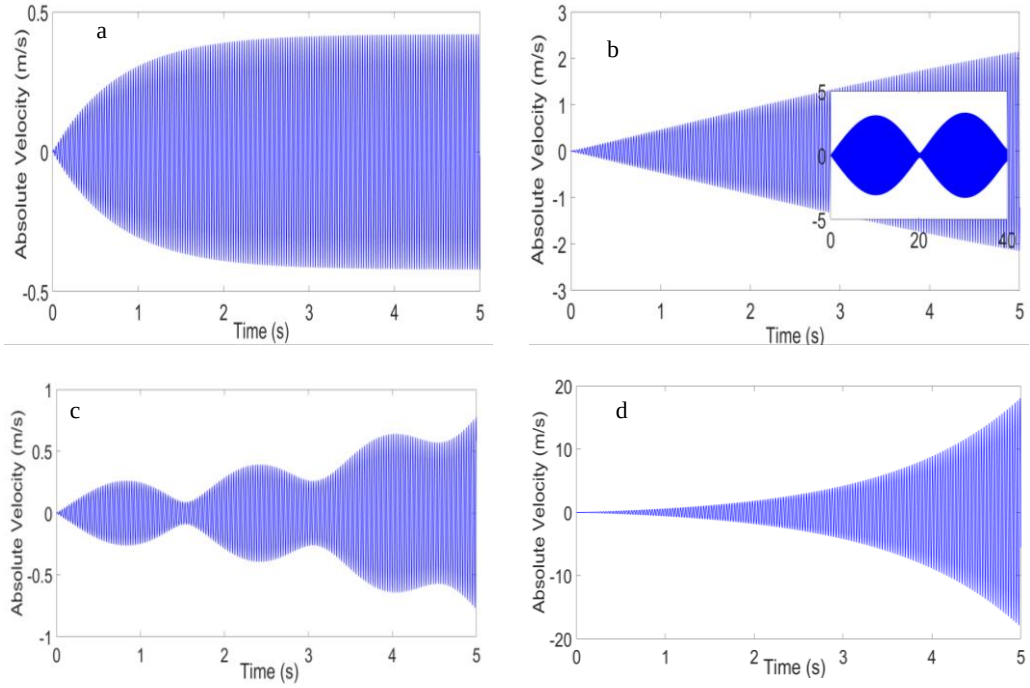

Fig.9. Evolution of the absolute velocity-time waveform signals using piezoelectric segment (L_1=0.09 m & L_2=0.06 m) and electrode segment (β_1-α_1=144º & β_2-α_2=144º) with R_d=100 kΩ and C_d = 0.1 μF under fluid velocity and resonance excitation: (a) U=6 m/s with 35.43 Hz, (b) U=6.97 m/s with 34.78 Hz, (c) U=7.25 m/s with 35.50 Hz, (d) U=7.48 m/s with 34.60 Hz.

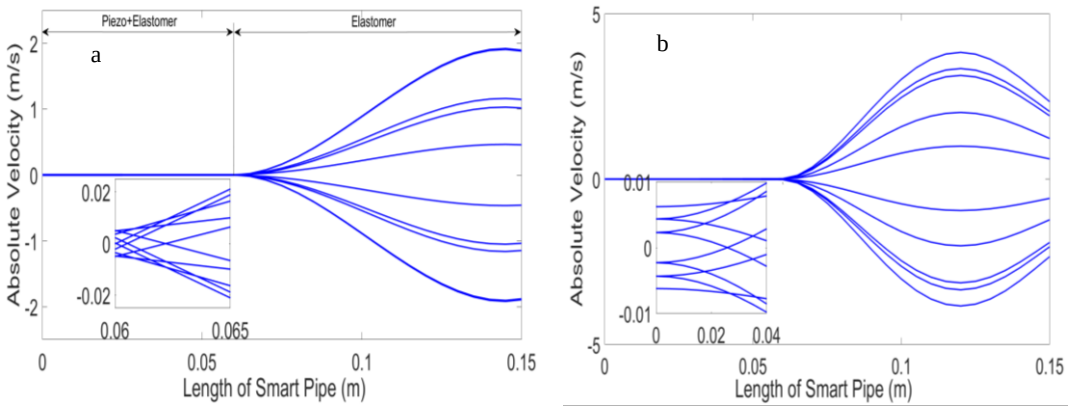

Fig.10. Dynamic evolution of the smart pipe structure over one period of the absolute velocity-time waveform signals using piezoelectric segment (L_1=0.06 m & L_2=0.09 m) and electrode segment (β_1-α_1=144º & β_2-α_2=144º) with R_d=100 kΩ, C_d = 0.1 μF, and U=5 m/s: (a) first coupled mode and (b) second coupled mode.

In Fig. 10, the physical motions of the elastic smart pipe using partially piezoelectric segment (L_1=0.06m & L_2=0.09m) show the dynamic evolution over one period of the absolute velocity-time waveform. The first two coupled modes of the particular resonance frequencies are shown as an example. Unlike the previous published works related to the fluid structure interaction, this paper shows the elastic pipe under base excitation where the absolute velocity phenomenon was chosen for the analysis. This can be proved that the base support of the elastic pipe does not completely give the fixed value of zero absolute velocity. For example, at some point for the first coupled mode, when the base support initially approaches positive maximum velocity, the tip end of the elastic pipe reaches minimum level of negative velocity. This occurs over half-period of the absolute velocity-time waveform. However, when the base support moves down at the negative velocity value, the tip end of the elastic pipe moves up at the positive velocity value. This situation occurs repetitively when the base support moves up and down at instant times. It is important to note here that the segment of L_1=0.06 m shows the lowest velocity due to the stiffness contribution of piezoelectric and elastomer. Although, the piezoelectric thickness is quite thin, its modulus of elasticity is very high compared with the elastomer. Moreover, the second coupled mode shows different dynamic evolution over one period of the absolute velocity-time waveform.

With the constant base excitation and variable flow velocity, the variable optimal power output can be visualised in Fig. 11 in order to identify the effect of the flow velocity on the pipe system. As shown, with increasing flow velocity, the optimal power output also increases until reaching its critical value. Then, the power gradually decreases as flow velocity increases further. Note that the system response as shown here only investigates the onset of instability. Nevertheless, the study can be utilised as an essential identification for dynamic instability. In future work, the nonlinear coupled system due to the flutter instability with a Hopf bifurcation will be considered. There is also some coupling between the frequency response and velocity signal behaviour due to flow velocity. As shown, a stable response below the critical flow velocity occurs where the velocity signal reaches a steady state. However, the beating signal will occur after reaching the critical flow velocity region. After the critical value, the flutter instability response occurs with increasing fluid velocities where the signal grows continuously with oscillation and without bound.

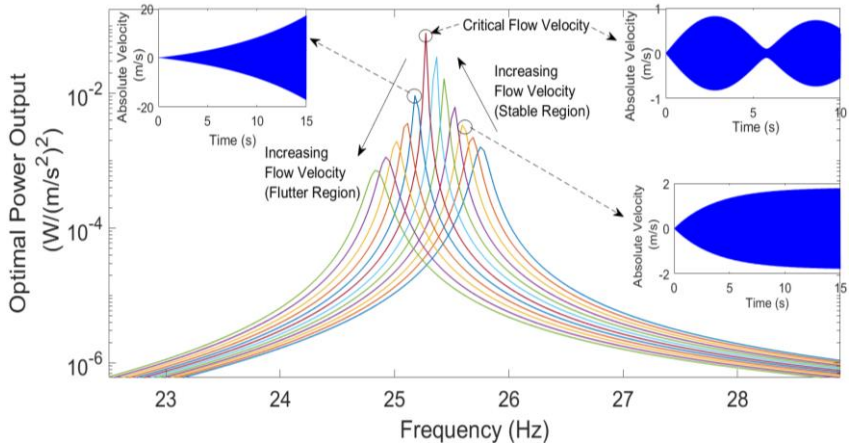

Fig.11. Optimal power harvesting FRFs under variable flow velocity using piezoelectric segment (L_1=0.06 m & L_2=0.09 m) and electrode segment (β_1-α_1=144º & β_2-α_2=144º)

The optimal power harvesting frequency response for the elastic pipe with the effects of the fluid and base excitation can be seen in Fig. 12. Note that the optimal power output can be obtained using the optimal load resistance as shown in Eq. (48). It obviously shows the trend of the first coupled mode response with variable flow velocity where it has relationship with the previous result. The stable response occurs at the variable resonance frequency. However, in the second coupled mode, the optimal power shows the unstable response by flutter. With increasing flow velocity, the maximum power of 0.08 W/(m.s^{-2})^2 can be achieved at critical flow velocity. Note that the optimal power at very high amplitude can still be achieved before reaching critical flow velocity. It only requires the lower flow velocity to reach its critical value. Also note that the resonance frequency will be different if the flow velocity changes. In such situation, this series of events shows of how the fluid flow amplifies the elastic pipe.

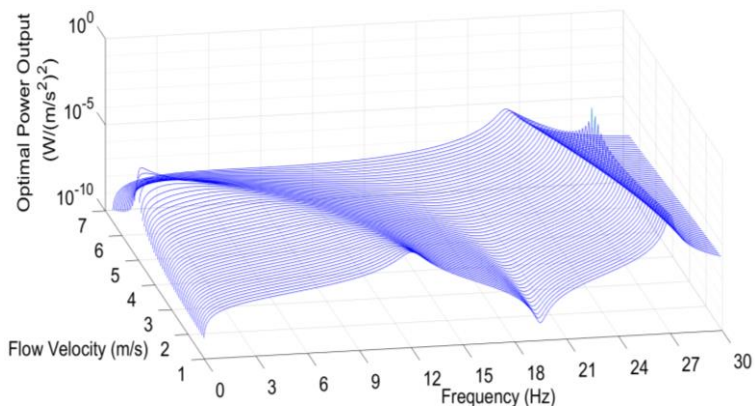

Fig.12. Optimal power harvesting FRFs at first and second coupled modes under variable flow velocity using piezoelectric segment (L_1=0.06 m & L_2=0.09 m) and electrode segment (β_1-α_1=144º & β_2-α_2=144º)

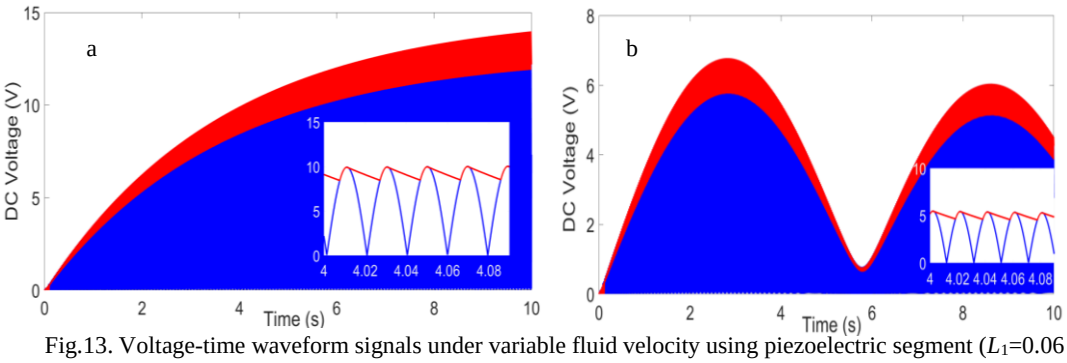

Fig.13. Voltage-time waveform signals under variable fluid velocity using piezoelectric segment (L_1=0.06 m & L_2=0.09m) and electrode segment (β_1-α_1=144° & β_2-α_2=144°) with R_d=100 kΩ and C_d = 0.1 μF (blue line: rectifier DC voltage and red line: capacitor DC voltage): (a) U=3.75 m/s and (b) U=4.06 m/s.

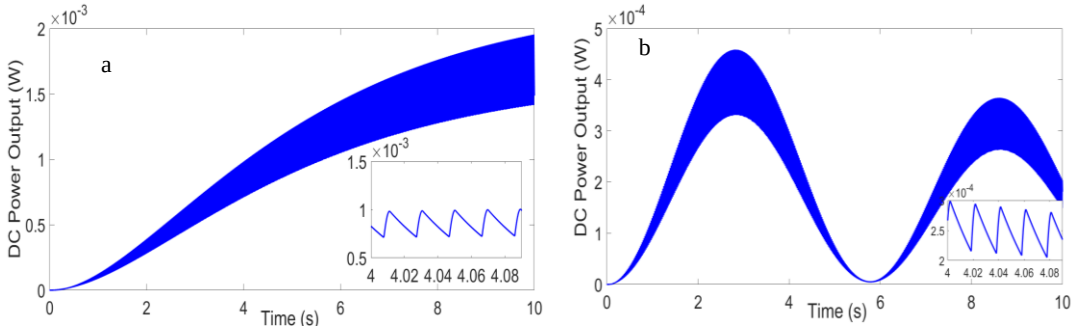

Fig.14. Power-time waveform signals using piezoelectric segment (L_1=0.06m & L_2=0.09m) and electrode segment (β_1-α_1=144° & β_2-α_2=144°) with R_d=100 kΩ and C_d = 0.1 μF under variable flow velocity: (a) U=3.75 m/s and (b) U=4.06 m/s.

As shown in Fig. 13, the examples of the DC voltage signal time waveforms show different trends for different flow velocities. In Fig. 13a, the DC voltage signals of the rectifier and capacitor become constant after reaching 4 seconds because the chosen flow velocity is slightly below its critical value. However, the beat signal occurs when the flow velocity was similar with its critical value as shown in Fig. 13b. Fig. 8b also shows this behaviour based on the absolute velocity signal. Again, the beating phenomenon may not be effective for harvesting applications. The beating response may occur when the resonance of the smart structure is similar with fluid system. In Fig. 14, the power outputs also show similar behaviour. Note that the voltage and power signal amplitudes with flow velocity being a slight away from its critical value can give potential benefit for this case. However, if the chosen flow velocity is quite far away from its critical velocity, the DC signal response with variable resonance frequency excitation will tend to form fully flutter.

5 Conclusion

This paper has presented the unified analytical approach of flow-induced vibrational smart pipe structure with tip mass offset under input base excitation. The extended charge-type-Hamiltonian mechanics has been used to develop the Ritz method-based weak form analytical approach. The electrode circumference segment system and partial piezoelectric segment of the elastic pipe were considered in the theoretical modelling. The reduced orthonormalised dynamic equations have shown the coupled field constitutive formulations representing the mechanical system (fluid and solid), electromechanical system (piezoelectricity), and electrical system (circuit interface). The equations can formulate the electromechanical multi-mode frequency and time signal waveform response equations. The proposed techniques can be used to analyse the onset of the flutter instability due to the coupled system responses of the fluid, solid, circuit, and electromechanical systems. There are six findings that can be highlighted:

1. The initial investigation without fluid effect was presented in order to observe the common trend of power harvesting frequency response using optimal load resistance. This showed similar trends to the previous published works. Also, it also showed more complete studies using partial piezoelectric segments and circumference electrode segments, and there are no previous works showing these cases.

2. With the effect of fluid flow, the first four coupled modes have been used to analyse the dynamic instability using the root locus responses obtained from the characteristic coupled field equations and the result of which have been displayed into the Argand diagram. It obviously becomes the essence of observing dynamic instability for each mode. We observed that the partially piezoelectric segments (L_1=0.06m & L_2=0.09 m) and (L_1=0.09m & L_2=0.06 m) with the electrode segment (β_1-α_1=144° & β_2-α_2=144°) showed the optimal response with the potential and effective options for the pipe conveying fluid for power harvesting applications. However, partially piezoelectric segments (L_1=0.06m & L_2=0.09m) was chosen for further analysis. Note that the circumference electrode segment was used due to avoiding the electric charge cancellation.
3. Each parametric case studies showed their relations to each other giving the validated proofs from the findings. For example, the results from the Argand diagram can be confirmed using the evolution of the absolute velocity-time waveform signals and the 3-D power harvesting frequency response with variable flow velocity.
4. Beating signal phenomena occurs at the critical flow velocity giving the maximum power output amplitude from the 3-D power harvesting frequency response. Beating signal responses were identified due to the resonance of the elastic pipe having a similar value with the fluid system. However, the beating signal may not be any benefit for DC power output-time waveform signals. Operating slightly away from the critical flow velocity can be an effective option for all scenarios of the studies.
5. The dynamic evolution for the first two coupled modes was also presented in order to show the behaviour of the physical motions of the smart pipe system (from the base support to the tip end).
6. The potential and effective options for the smart pipe conveying fluid for power harvesting applications depend on the optimal responses, lower onset of flutter instability, and lower critical velocity value and beyond (Hopf bifurcation). A smart pipe having a divergent instability may not be good choice since its natural dynamic behaviour shows static instability that gives a pipe velocity growing continuously without oscillation.

Appendix A. Modified Elastic Constant and Piezoelectric Constant

The modified elastic constant and piezoelectric constant for piezoelectric layer can be formulated, respectively as,

$$\bar{c}_D^{(2)} = \bar{c}_{11}^{(2,E)} + e_{31}^{(2)2}\varepsilon_{33}^{(2,S)^{-1}}, \quad g_{31}^{(2)} = \varepsilon_{33}^{(2,S)^{-1}} e_{31}^{(2)} . \tag{A.1}$$

The permittivity at constant strain (superscript S) represents $\varepsilon_{33}^{(2,S)} = \varepsilon_{33}^{(2,T)} - d_{31}^2 c_{11}^{(2,E)}$ where $\varepsilon_{33}^{(2,T)}$ is the permittivity at constant stress (superscript T).

Appendix B. Stiffness Coefficients for the Smart Pipe Structure

The total transverse stiffness coefficient for the first and second segments can be formulated as,

$$C_{t1} = \frac{\pi}{2}\left(\left(r_2^{\,4} - r_1^{\,4}\right)\bar{c}_{11}^{(1)} + \left(r_3^{\,4} - r_2^{\,4}\right)\bar{c}_D^{(2)}\right), \; C_{t2} = \frac{\pi}{2}\left(r_2^{\,4} - r_1^{\,4}\right)\bar{c}_{11}^{(1)} \quad . \tag{B.1}$$

Appendix C. Mass Moment of Inertias for the Smart Pipe Structure and Proof Mass Offset

The zeroth mass moment of inertias for the first and second segments of smart structure can be formulated as,

$$I_{01} = \pi\left(\left(r_2^{\,2} - r_1^{\,2}\right)\rho^{(1)} + \left(r_3^{\,2} - r_2^{\,2}\right)\rho^{(2)}\right), \quad I_{02} = \pi\rho^{(1)}\left(r_2^{\,2} - r_1^{\,2}\right) \; . \tag{C.1}$$

The zeroth mass moment of inertia of the proof mass offset can be formulated as,

$$I_0^{tip} = \pi\, l_t\left(\left(r_t^{\,2} - r_3^{\,2}\right)\rho_t + \left(r_2^{\,2} - r_1^{\,2}\right)\rho^{(1)} + \left(r_3^{\,2} - r_2^{\,2}\right)\rho^{(2)}\right). \tag{C.2}$$

The second mass moment of inertia of the proof mass offset at the point d in Fig. 2 can be formulated as,

$$I_2^{tip} = \frac{\pi\, l_t}{12}\left(\left(3\left(r_t^{\,4} - r_3^{\,4}\right) + l_t^{\,2}\left(r_t^{\,2} - r_3^{\,2}\right)\right)\rho_t + \left(3\left(r_2^{\,4} - r_1^{\,4}\right) + l_t^{\,2}\left(r_2^{\,2} - r_1^{\,2}\right)\right)\rho^{(1)} + \left(3\left(r_3^{\,4} - r_2^{\,4}\right) + l_t^{\,2}\left(r_3^{\,2} - r_2^{\,2}\right)\right)\rho^{(2)}\right)$$
$$+ \frac{\pi\, l_t^{\,3}}{4}\left(\left(r_t^{\,2} - r_3^{\,2}\right)\rho_t + \left(r_2^{\,2} - r_1^{\,2}\right)\rho^{(1)} + \left(r_3^{\,2} - r_2^{\,2}\right)\rho^{(2)}\right). \tag{C.3}$$

Note that, Eqs. (C.2)-(C.3) show mass moment of inertias for the whole proof mass because the attached proof mass offset is a rigid body that perfectly bonded with the portion of the smart pipe structure.

Appendix D. Modified Transverse Piezoelectric Coupling Coefficient and Modified Piezoelectric Internal Capacitance

Modified transverse piezoelectric couplings for the first and second electrode segments in the harvesting piezoelectric layer can be formulated, respectively as,

$$\eta_1 = \frac{g_{31}^{(1)}\left(r_3{}^3 - r_2{}^3\right)\left(-\cos\beta_1 + \cos\alpha_1\right)}{3r_3 L_1\left(\beta_1 - \alpha_1\right)} \;,\; \eta_2 = -\frac{g_{31}^{(1)}\left(r_3{}^3 - r_2{}^3\right)\left(-\cos\beta_2 + \cos\alpha_2\right)}{3r_3 L_1\left(\beta_2 - \alpha_2\right)} \;. \tag{D.1}$$

Note that the negative sign on the second part of Eq. (D1) is due to the opposite polarisation direction of the lower part of cross-sectional pipe. The modified internal capacitances can be stated, respectively as,

$$C_{v1} = \frac{2\varepsilon_{33}^S r_3{}^2 L_1\left(\beta_1 - \alpha_1\right)}{\left(r_3{}^2 - r_2{}^2\right)} \quad , \quad C_{v2} = \frac{2\varepsilon_{33}^S r_3{}^2 L_1\left(\beta_2 - \alpha_2\right)}{\left(r_3{}^2 - r_2{}^2\right)} \,. \tag{D.2}$$

Also note that the two segmented electrodes located at the particular regions of the piezoelectric pipe give different internal capacitances which depend on the angle (in radian) of those regions in the polar coordinate system.

Appendix E. Mode Shapes of Partially Cantilevered Pipe Structure with Proof Mass Offset

The two mechanical dynamic equations for partially pipe structures can be formulated as,

$$I_{01}\ddot{w}_1(x,t) + C_{t1}\frac{\partial^2}{\partial x^2}\left(\frac{\partial^2 w_1(x,t)}{\partial x^2}\right) = 0 \,,\quad I_{02}\ddot{w}_2(x,t) + C_{t2}\frac{\partial^2}{\partial x^2}\left(\frac{\partial^2 w_2(x,t)}{\partial x^2}\right) = 0 \;. \tag{E.1}$$

The static boundary conditions are given as,

$$w_1(0,t) = 0 \quad , \quad \frac{\partial w_1(0,t)}{\partial x} = 0 \,. \tag{E.2}$$

The transition boundary conditions are shown as,

$$w_1(L_1,t) = w_2(0,t), \quad \frac{\partial w_1(L_1,t)}{\partial x} = \frac{\partial w_2(0,t)}{\partial x}, \tag{E.3}$$

$$C_{t1}\frac{\partial}{\partial x}\left(\frac{\partial^2 w_1(L_1,t)}{\partial x^2}\right) = C_{t2}\frac{\partial}{\partial x}\left(\frac{\partial^2 w_2(0,t)}{\partial x^2}\right), \quad C_{t1}\frac{\partial^2 w_1(L_1,t)}{\partial x^2} = C_{t2}\frac{\partial^2 w_2(0,t)}{\partial x^2} \,. \tag{E.4}$$

The dynamic boundary conditions can be formulated as,

$$x_c I_0^{tip}\frac{\partial \ddot{w}_2(L_2,t)}{\partial x} + I_0^{tip}\ddot{w}_2(L_2,t) - C_{t2}\frac{\partial}{\partial x}\left(\frac{\partial^2 w_2(L_2,t)}{\partial x^2}\right) = 0 \,, \tag{E.5}$$

$$I_2^{tip}\frac{\partial \ddot{w}_2(L_2,t)}{\partial x} + x_c I_0^{tip}\ddot{w}_2(L_2,t) + C_{t2}\frac{\partial^2 w_2(L_2,t)}{\partial x^2} = 0 \,. \tag{E.6}$$

The method of separation of variables $w(x,t) = W_k(x)y(t)$ was used where the general solutions of mode shapes for each segment as shown in Fig. 1 can be formulated as,

$$W_k(x) = \begin{cases} W_{k1}(x) = A_1\cos\mu x + B_1\sin\mu x + C_1\cosh\mu x + D_1\sinh\mu x \;,\; 0 \le x \le L_1 \\ W_{k2}(x) = A_2\cos\beta x + B_2\sin\beta x + C_2\cosh\beta x + D_2\sinh\beta x \;,\; 0 \le x \le L_2 \end{cases} \;. \tag{E.7}$$

Using Eq. (E7) into Eqs. (E2)-(E7), the characteristic equations in the matrix form can be solved giving the frequency equations μ and $\beta = \sqrt[4]{\mu^4 I_{02}C_{t1}/\left(I_{01}C_{t2}\right)}$ including the unknown constants. Eq. (E7) with the eight constants must be algebraically simplified to give only one similar constant for both mode shapes. Once the modified Eq. (E7) was obtained, the equal constant was presumed to be one because the orthonormalisation-based Ritz method and its Ritz constants were utilised, such that the Ritz eigenfunction showed the accurate mode shapes.

References

1. Feodos'ev, V.P.: Vibrations and stability of a pipe when liquid flows through it. Inzhenernyi Sbornik, **10**, 1013-1024 (1951)
2. Housner, G.W.: Bending vibrations of a pipe line containing flowing fluid. J. App. Mech, **19**, 205-208 (1952)
3. Niordson, F.I.: Vibrations of a cylindrical tube containing flowing fluid. Kungliga Tekniska Hogskolans Handlingar (Stockholm) No. 73 (1953)
4. Holmes,P.J., Pipes supported at both ends cannot flutter. J. App. Mech., 1978, 45: 619-622.
5. Heinrich, G.: Schwingungen durchströmter Rohre (Vibrations of pipes with flow), Zeitschrift für Angewandte Mathematik und Mechanik, **36**, 417-427 (1956)
6. Benjamin, T.B.: Dynamics of a system of articulated pipes conveying fluid. I. Theory. Proceedings of the Royal Society (London) A, **261**, 457-486 (1961)
7. Benjamin, T.B.: Dynamics of a system of articulated pipes conveying fluid. II. Experiments. Proceedings of the Royal Society (London) A, **261**, 487-499 (1961)
8. Bottema, O.: On the stability of equilibrium of a linear mechanical system, Zeitschrift für Angewandte Mathematik und Mechanik, **6**, 97-104 (1955)
9. Smith, T. E., Herrmann, G.: Stability of circulatory elastic systems in the presence of magnetic damping, Acta Mech.**12**, 175-188 (1971)
10. Gregory, R.W., Païdoussis, M.P.: Unstable oscillation of tubular cantilevers conveying fluid. I. Theory. Proceedings of the Royal Society (London) A, **293,** 512-527 (1966)
11. Gregory, R.W. Païdoussis, M.P.: Unstable oscillation of tubular cantilevers conveying fluid. II. Theory. Proceedings of the Royal Society (London) A, **293**, 528-542 (1966)
12. Sokolnikoff, I.S.: Mathematical theory of elasticity, 2nd Edition McGraw-Hill (1956)
13. Païdoussis, M.P., Issid, N.T.: Dynamic stability of pipes conveying fluid. J. Sound Vib. **33**, 267-294 (1974)
14. Païdoussis, M.P. Li, G.X.: Pipes conveying fluid: a model dynamical problem. J. Fluids. Struct. **7**, 137–204 (1993)
15. Ruta, G.C., Elishakoff, I.: Towards the resolution of the Smith–Herrmann paradox. Acta Mech. **173**, 89–105 (2004)
16. De Bellis, M.L., Ruta, G.C., Elishakoff, I.: A contribution to the stability of an overhanging pipe conveying fluid. Continuum Mech. Thermodyn. **27**, 685–701 (2015)
17. Gorman, D.G., Reese, J.M., Zhang, Y.L.: Vibration of a flexible pipe conveying viscous pulsating fluid flow. J. Sound Vib. **230**, 379-392 (2000)
18. Lee, U., Pak C.H., Hong, S.C.: The dynamics of a piping system with internal unsteady flow. J. Sound Vib. **180** (2):297–311 (1995)
19. Lavooij , C.S.W., Tijsseling, A.S.: Fluid–structure interaction in liquid-filled piping systems. J. Fluids. Struct. **5**, 573–95 (1991).
20. Zhang , Y.L., Gorman, D.G., Reese, J.M.: Analysis of the vibration of pipes conveying fluid. J. Mech. Eng. Sci. **213**, 849–60 (1999)
21. Wadham-Gagnon, M., Païdoussis, M.P., Semler, C.: Dynamics of cantilevered pipes conveying fluid, part 1: nonlinear equations of three dimensional motion. J. Fluids Struct. **23**, 545–567 (2007)
22. Païdoussis, M.P., Semler, C., Wadham-Gagnon, M.: Dynamics of cantilevered pipes conveying fluid. Part 2: dynamics of the system with intermediate spring support. J. Fluids Struct. **23** 569–587 (2007)
23. Modarres-Sadeghi, Y., Semler, C., Wadham-Gagnon, M., Païdoussis, M.P.: Dynamics of cantilevered pipes conveying fluid. Part 3: three dimensional dynamics in the presence of an end-mass. J. Fluids Struct. **23**, 589–603 (2007)
24. Païdoussis, M.P., Fluid-Structure Interactions: Slender Structures and Axial Flow, vol. 1, Academic Press, London, the 2nd Edition (2014).
25. Pai'doussis, M.P:. Aspirating pipes do not flutter at infinitesimally small flow. J. Fluids Struct. **13**, 419-425 (1999)
26. Kuiper, G.L., Metrikine, A.V.: Dynamic Stability of a Submerged, Free-Hanging Riser Conveying Fluid. J. Sound Vib. **280**, 1051–1065 (2005)
27. Païdoussis, M.P., Semler, C. Wadham-Gagnon, M.: A Reappraisal of Why Aspirating Pipes do not Flutter at Infinitesimal Flow. J. Fluids Struct. **20**, 147–156 (2005)
28. Kuiper, G.L. Metrikine, A.V.: Experimental Investigation of Dynamic Stability of a Cantilever Pipe Aspirating Fluid. J. Fluids Struct. **24**, 541–558 (2008)

29. Giacobbi, D. B., Rinaldi, S., Semler, C., Païdoussis, M.P.: The dynamics of a cantilevered pipe aspirating fluid studied by experimental, numerical and analytical methods, J. Fluids Struct. **30**, 73-96 (2012)
30. Krommer, M., Irschik, H.: An electromechanically coupled theory for piezoelastic beams taking into account the charge equation of electrostatics. Acta Mech. **154**, 141–158 (2002)
31. Krommer,M.: On the correction of the Bernoulli–Euler beam theory for smart piezoelectric beams. Smart Mater. Struct.**10**, 668–680 (2001)
32. Fernandes, A., Pouget J.: Analytical and numerical approach to piezoelectric bimorph. Int. J. Solids Struct. **40,** 4331–52 (2003)
33. Moita, J.M., Correia, I.F.P., Soares, C.M.M.: Active control of adaptive laminated structures with bounded piezoelectric sensors and actuators. Comput. Struct. **82** (17-19) 1349-58 (2004)
34. Irschik, H., Ziegler, F.: Eigenstrain without stress and static shape control of structures. AIAA J. **39**, 1985-1990 (2001)
35. Irschik, H., Krommer, M., Belyaev, A.K., Schlacher, A.K.: Shaping of piezoelectric sensors/actuators for vibrations of slender beams: coupled theory and inappropriate shape functions. J. Intell. Mater. Syst. Struct. **9**, 546–554 (1998)
36. Irschik, H.; Krommer, M.; Pichler, U.: Dynamic shape control of beam-type structures by piezoelectric actuation and sensing. Int. J. Appl. Electromagn. Mech. **17**, 251-258. (2003)
37. Irschik,H.; Pichler,U. Dynamic shape control of solids and structures by thermal expansion strains. J. Therm. Stresses, **24**, 565-576 (2001)
38. Krommer, M., Zellhofer, M., Heilbrunner, K.-H.: Strain-type sensor networks for structural monitoring of beam-type structures. J. Intell. Mater. Syst. Struct. **20**, 1875–1888 (2003)
39. Krommer, M.; Vetyukov, Yu.: Adaptive sensing of kinematic entities in the vicinity of a time-dependent geometrically nonlinear pre-deformed state. Int. J. Solid. Struct. **46**, 3313-3320 (2009)
40. Kapuria, S., Yasin, M.Y.: Active vibration control of smart plates using directional actuation and sensing capability of piezoelectric composites. Acta Mech. **224**, 1185–1199 (2013)
41. Tzou, H.S., Tseng, C.I.: Distributed vibration control and identification of coupled elastic/piezoelectric systems: finite element formulation and applications. Mech. Syst. Signal Process. **5**, 215–231 (1991)
42. Krommer, M., Irschik,H.: A Reissner-Mindlin-type plate theory including the direct piezoelectric and the pyroelectric effect. Acta Mech. **141**, 51–69 (2000)
43. Krommer, M.: On the influence of pyroelectricity upon thermally induced vibrations of piezothermoelastic plates. Acta Mech. **171**, 59–73 (2004)
44. dell'Isola, F., Maurini, C., Porfiri, M.: Passive damping of beam vibrations through distributed electric networks and piezoelectric transducers: prototype design and experimental validation. Smart Mater. Struct. **13**, 299–308 (2004)
45. Niederberger, D., Morari, M.: An autonomous shunt circuit for vibration damping. Smart Mater. Struct. **15**, 359–364 (2006)
46. Schoeftner, J., Krommer, M.: Single point vibration control for a passive piezoelectric Bernoulli-Euler beam subjected to spatially varying harmonic loads. Acta Mech. **223**, 1983–1998 (2012)
47. Vasques, C.M.A.: Improved passive shunt vibration control of smart piezo-elastic beams using modal piezoelectric transducers with shaped electrodes. Smart Mater. Struct. **21**, 125003 (2012)
48. Liao Y and Sodano H 2010 Modeling and comparison of bimorph power harvesters with piezoelectric elements connected in parallel and series. J. Intell. Mater. Syst. Struct. **21** 149–159 (2010)
49 Goldschmidtboeing, F., Woias P.: Characterization of different beam shapes for piezoelectric energy harvesting J. Micromech. Microeng. **18** 104013 (2008)
50. Kim, M., Hoegen, M., Dugundji, J., Wardle, B.L.:Modeling and experimental verification of proof mass effects on vibration energy harvester performance. Smart Mater. Struct. **19** 045023 (2010)
51 Dalzell, P., Bonello, P.: Analysis of an energy harvesting piezoelectric beam with energy storage circuit Smart Mater. Struct. **21**105029 (2012)
52. Lumentut, M.F., Howard, I.M. Analytical and experimental comparisons of electromechanical vibration response of a piezoelectric bimorph beam for power harvesting. Mech. Syst. Signal Proc. **36** 66–86 (2013)

53. Lumentut, M.F., Howard, I.M.: Parametric design-based modal damped vibrational piezoelectric energy harvesters with arbitrary proof mass offset: numerical and analytical validations. Mech. Syst. Signal Process. 68–69, 562–586 (2016)
54. Adhikari, S., Friswell, M.I., Inman, D.J.: Piezoelectric energy harvesting from broadband random vibrations. Smart Mater. Struct. **18** 115005 (2009)
55. Ali, S.F., Friswell, M.I., Adhikari, S.: Piezoelectric energy harvesting with parametric uncertainty, Smart Mater. Struct. **19**, 105010 (2010)
56. Lumentut, M.F., Howard, I.M.: Intrinsic electromechanical dynamic equations for piezoelectric power harvesters. Acta Mech. **228** (2), 631–650 (2017)
57. Friswell, M.I., Adhikari, S.: Sensor shape design for piezoelectric cantilever beams to harvest vibration energy. J. App. Phy. **108**, 014901 (2010)
58. Lumentut, M.F., Howard, I.M.: Electromechanical finite element modelling for dynamic analysis of a cantilevered piezoelectric energy harvester with tip mass offset under base excitations. Smart Mater. Struct. **23**, 095037 (2014)
59. Tang, L., Wang, J.: Size effect of tip mass on performance of cantilevered piezoelectric energy harvester with a dynamic magnifier, Acta Mech. **228**(11), 3997–4015 (2017)
60. Karami, A., Inman, D.J.: Electromechanical modeling of the low frequency zigzag micro energy harvester. J. Intell. Mat. Syst. Struct. **22**(3), 271-282 (2011)
61. Zhou, S., Hobeck, J.D., Cao, J., Inman, D.J.: Analytical and experimental investigation of flexible longitudinal zigzag structures for enhanced multi-directional energy harvesting Smart Mater. Struct. **26**, 035008 (2017)
62. Lumentut, M.F., Francis, L.A., Howard, I.M.: Analytical techniques for broadband multielectromechanical piezoelectric bimorph beams with multifrequency power harvesting. IEEE Trans. Ultrason. Ferroelectr. Freq. Control, **59**, 1555-68 (2012)
63. Zhang, H., Afzalul, K.: Design and analysis of a connected broadband multi-piezoelectric-bimorph-beam energy harvester. IEEE Trans. Ultrason. Ferroelectr. Freq. Control, **61** 1016-1023 (2014)
64. Lien, I.C., Shu, Y.C., Wu, W.J., Lin, H.C.: Revisit of series-SSHI with comparisons to other interfacing circuits in piezoelectric energy harvesting. Smart Mater. Struct. **19** 125009 (2010)
65. Lin, H.C., Wu, P.H, Lien, I.C., and Shu, Y.C.: Analysis of an array of piezoelectric energy harvesters connected in series. Smart Mater. Struct. **22** 094026 (2013)
66. Wu, P.H., Shu, Y.C.: Finite element modeling of electrically rectified piezoelectric energy harvesters Smart Mater. Struct. **24**, 094008 (2015)
67. Lumentut, M.F., Howard, I.M.: Effect of shunted piezoelectric control for tuning piezoelectric power harvesting system responses—analytical techniques. Smart Mater. Struct. **24**, 105029 (2015)
68. Lumentut, M.F., Howard, I.M.: Electromechanical analysis of an adaptive piezoelectric energy harvester controlled by two segmented electrodes with shunt circuit networks. Acta Mech. **228**(4), 1321–1341 (2017)
69. Hobbs, W.B., Hu, D. L.: Tree-inspired piezoelectric energy harvesting. J. Fluids Struct. **28**, 103–114 (2012)
70. Barrero-Gil, A., Alonso, G., Sanz-Andres, A.: Energy harvesting from transverse galloping. J. Sound Vib. **329** (24) 2873–2883 (2010)
71. Hémona, P., Amandolesea, X., Andriannec, T.: Energy harvesting from galloping of prisms: A wind tunnel experiment. J. Fluids Struct. **70**, 390-402 (2017)
72. Michelin, S., Doaré, O.: Energy harvesting efficiency of piezoelectric flags in axial flows. J. Fluid Mech. **714**, 489–504 (2013)
73. Nye, J.F.: Physical properties of crystals: their representation by tensors and matrices, Oxford, England: Clarendon Press (1984)
74. Ikeda, T.: Fundamentals of Piezoelectricity. Oxford University Press, New York (1990)
75. Tichý, J.,Erhart, J.,Kittinger, E.,Prívratská, J.: Fundamentals of Piezoelectric Sensorics. Springer, Berlin, Heidelberg (2010)
76. Ritz, W.: Über eine neue Methode zur Lösung gewisser Variationsprobleme der mathematischen Physik. Journal für die Reine und Angewandte Mathematik **135** 1–61 (1909)
77. Courant R and Hilbert D 1953-1962 Methoden der mathematischen physik / English Ed.: Methods of mathematical physics (New York : Interscience Publishers)